Integrating UAV Imagery with Traditional Fieldwork for Multi-Scale Analysis of Natural Fracture Networks: A Case Study of the Parmelan Plateau

Stamena Zekic

Delft University of Technology

Integrating UAV Imagery with Traditional Fieldwork for Multi-Scale Analysis of Natural Fracture Networks: A Case Study of the Parmelan Plateau

by

Stamena Zekic

to obtain the degree of Master of Science
in Applied Earth Sciences
at Delft University of Technology,
to be defended publicly on 19.09.2024.

Student number:	4525744
Supervisor:	Dr. P-O.B.R. Bruna
Supervisor:	Msc. J. Hupkes
Committee:	Prof. Dr. G. Bertotti
Committee:	Dr. A. Barnhoorn
Faculty:	Faculty of Civil Engineering and Geosciences, Delft
Course name:	AESM2310 - Final Thesis Geo-Energy Engineering

Cover: Parmelan. Photograph by Stamena Zekic.

An electronic version of this thesis is available at `http://repository.tudelft.nl/`.

TU Delft   Molengraaff Fund   FAST TU Delft University Fund

Abstract

This thesis attempts to evaluate the extent to which UAV imagery can complement traditional geological fieldwork and to assess the behaviour of natural fracture networks across multiple scales. By conducting detailed field surveys and capturing high-resolution UAV images, the study provides a comprehensive comparison of the data, particularly in terms of fracture orientations, lengths, density, intensity and topology. The Parmelan plateau in France has been studied as a potential geothermal reservoir analogue. This study utilises an integrated approach combining fieldwork, high-resolution Unmanned Aerial Vehicle (UAV) imagery, and satellite imagery.

Field data collected using field scanlines were compared with data obtained from UAV imagery to evaluate the efficacy of each approach. The results indicate that UAV imagery, while advantageous for covering large and inaccessible areas, faces significant limitations in accurately identifying fracture types and orientations without supplementary field data. This discrepancy is primarily attributed to factors such as image resolution - limited visibility of small-scale fracture-type indicators.

The multi-scale analysis performed in this study shows that natural fracture networks exhibit similar behaviour across different scales, though some scale-dependent variations are evident. The findings highlight the importance of integrating UAV data with traditional field methods to achieve a better understanding of fracture networks. This integration is particularly important for optimizing outcrop analogue data used in modelling subsurface geothermal reservoirs, which can significantly enhance the efficiency of geothermal energy extraction.

Preface

I would like to express my gratitude to everyone who has guided me through this process. I especially want to thank my supervisor, Pierre-Olivier Bruna, for his support, constructive criticism and advice throughout this project. I would also like to thank Jasper Hupkes for his invaluable assistance and for being a great companion in the field. Moreover, I would like to express my gratitude to Giovanni Bertotti for his feedback and advice. The fieldwork would not have been possible without the financial support of the Molengraaff Fund and FAST fund. I am grateful to everyone involved in awarding these funds. I sincerely appreciate my friends and fellow students in the department, whose insightful discussions and moral support were crucial in moments of difficulty.

Lastly I would like to thank my family, friends and roommates for always standing by me throughout this challenging process.

Stamena Zekic
Delft, September 2024

Contents

1 Introduction

Geothermal energy, characterized by minimal greenhouse gas emissions, plays an important role in the energy transition. It is considered a renewable and sustainable energy source, where hot water is pumped from a reservoir rock deep under the surface. After the heat is extracted, the water is re-injected into the reservoir. The efficiency of geothermal energy production heavily depends on the porosity of these reservoir rocks. If the reservoir rocks have low primary porosity and permeability, the flow of the fluids in the subsurface will be limited. In this case, the flow could be carried by natural fractures. If present in the rock, natural fractures must be open and connected to transport fluid. Therefore, understanding the spatial arrangement of interconnected or disconnected fractures, natural fracture networks, in the subsurface is essential for optimising geothermal energy production in low-porosity reservoirs.

Natural fracture networks are usually studied from outcrops, borehole data (logging and core analysis) and seismic data. Extensive research is focused on borehole and seismic data (De Joussineau et al. 2016, Ray et al. 2012, Daniau et al. 2008, Boersma et al. 2019). In the industry, static reservoir and fracture models are generally constructed using data from seismic surveys, well logs and core samples. Seismic data can provide large-scale information about the reservoir structure (km-scale faults for example) but with low resolution and high uncertainty. However, fractures are often not visible at seismic scale. Well and core data can provide high-resolution information about the reservoir properties, but the spatial coverage is limited - 1D information (figure 1.1). The resolution discrepancy between these datasets is significant, differing by orders of magnitude (figure 1.1). This scarcity of subsurface data creates a critical gap in our comprehensive understanding of the subsurface. However, natural fracture networks can be studied in detail over scales from 10^{-1}m to 10^{4}m from outcrops (Hardebol et al. 2015). Outcrop analogue studies can be used to bridge this resolution gap. Detailed quantitative analysis of outcrops can provide valuable predictive tools, and therefore minimize exploration and production risks (Bertotti et al. 2014).

Studying fractures from outcrop analogues can be done through various methods, including direct field measurements of fracture orientation and aperture (scanlines/scanareas), LIDAR scanning, and aerial photogrammetry (unmanned aerial vehicles (UAVs)). Traditional fieldwork involves manual data collection, providing detailed descriptions and precise measurements. On the other hand, ground work is a close-up of the network, it does not capture the complexity of it. Furthermore, it can be very time-consuming and labour-intensive, with inaccessible or dangerous study areas.

In this report, we studied if these limitations could be overcome using UAV imagery. UAVs are capable of taking high-resolution images over large areas in a short time and across inaccessible areas. The question is whether data quality can match the traditional fieldwork study.

Also, it is important to recognize that outcrops, which are surface exposures of subsurface rocks, have undergone at least one phase of exhumation. This exhumation, along with associated diagenetic processes, could lead to differences between outcrop analogues and the actual subsurface reservoir rocks

(Meda et al. 2019).

In this report we take Parmelan plateau (France), a low-porosity carbonate anticline, as an outcrop analogue for subsurface reservoirs exhibiting fracture-dominated permeability.

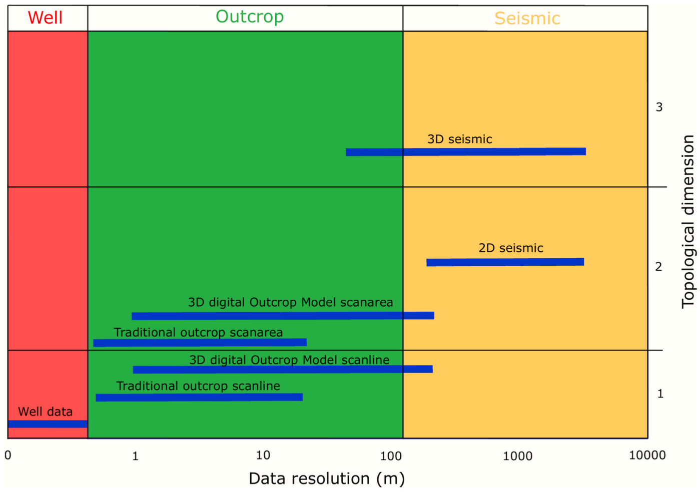

Figure 1.1: Diagram representing different observation scales. From Martinelli et al. 2020

The parameters studied in this report are important for fracture network connectivity and therefore for the fluid flow in a reservoir. For example, variability in orientation (multiple sets) increases the number of fracture intersections (figure 1.2 a) and b)); longer fractures increase the probability of intersection (figure 1.2 c), d), e) and d)); and higher density and intensity increase connectivity of a network (figure 1.2 g) and f)). Topology, unlike the previous parameters, is a scale-independent fracture network characteristic (Ovaskainen et al. 2023). It describes the relationship of fracture intersections. Depending on the type of intersection, overall fracture network connectivity can be determined. For example, a higher concentration of X and Y nodes increases the network connectivity compared to I nodes (further explained in Chapter 4).

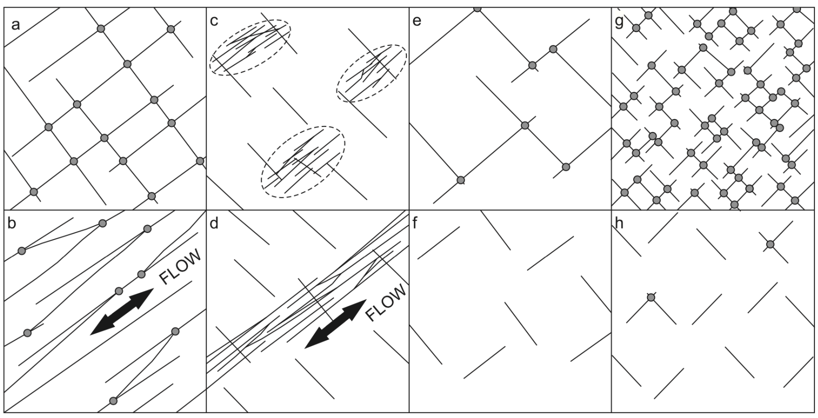

Figure 1.2: Fracture network connectivity dependence on different parameters: a) and b)variability in orientation (multiple sets) increases the number of intersections; c), d), e) and d) longer fractures increase the probability of intersection; and g) and f) higher density and intensity increase connectivity of a network. From Watkins et al. 2015.

1.1. Thesis objective

Satellite, high-resolution UAV data, scanline and field observation data of the Parmelan plateau, France, were analysed and interpreted, aiming to understand the natural fracture network variability across multiple scales. This report aims to answer the following research questions:

- How can UAV imagery enhance the use of outcrop analogue data and complement traditional fieldwork?
- Do natural fracture networks show consistent patterns across different scales, allowing for predictive modelling of their geometry?

The Parmelan plateau is located within the Geneva Basin, a region of great geological interest due to its potential for geothermal energy production. A project, 'The GEothermie2020 Program', led by the State of Geneva and and the Services Industriels de Genève7, aims to provide power and heating to the Geneva Canton, to reach the energy transition goals (Lecompte 2019). At the Parmelan plateau Lower Cretaceous limestones are exposed. This unit has already been identified as a regional aquifer (Clerc et al. 2015), a potential low enthalpy reservoir.

This report aims to give guidelines for the optimization of outcrop analogue data for fracture network prediction in subsurface geothermal reservoirs. Furthermore, it aims to understand the behaviour of fracture networks at different scales - if repetition of certain behaviour can be observed (for example if fracture networks indicate fractal behaviour).

To do this, a 2-week geological fieldwork in Parmelan (France) was conducted. During these two weeks, field data was collected for this project. Five parameters have been analysed on multiple scales: fracture orientation, length, intensity, density and topology.

1.2. Report Outline

The report consists of 8 chapters. Chapter 2 outlines general information on fractures and natural fracture networks. The following chapter describes the geological setting of the study area. In Chapter 4 the project workflow is discussed, as well as methods and available data. Furthermore, the fieldwork is outlined here. Chapter 5 gives the results of fieldwork vs UAV data comparison. Fracture orientation and length were studied. The next chapter presents the results of multi-scale fracture analysis. Chapter 7 discusses the results and outlines the uncertainties and limitations of the study. Finally, chapter 8 summarizes and concludes the findings.

2
Natural Fracture Networks

Natural fracture networks result from (semi-)brittle deformation of rock due to stress and strain. These fractures play a crucial role in the behaviour and properties of rocks, influencing fluid flow (Lei et al. 2020) and mechanical strength (Gale et al. 2010). Geometric attributes of fracture networks, such as fracture length and density (Berkowitz et al. 2000), topology (Sanderson and Nixon 2015), orientation distribution (Manzocchi 2002), and fracture spacing (Bai and Pollard 2000) are studied and analysed to characterise properties like spatial distribution (Corrêa et al. 2022, Marrett et al. 2018, Prabhakaran et al. 2021) scale and heterogeneity (Sweeney et al. 2023) of fracture networks, mechanical properties (Boersma et al. 2018) and in-situ stresses (Wang et al. 2021) of reservoir rocks, etc. Understanding these properties is important for the prediction of natural fracture networks in the subsurface and for developing reliable models.

2.1. Fracture Classification

Fractures can be described as discontinuities in a rock. Based on the nature of displacement, fractures are divided into: mode I (opening) and mode II (shearing) fractures. Additionally, two more types of discontinuities are considered: stylolites (closing-mode), and hybrid fractures (Ramsey and Chester 2004).

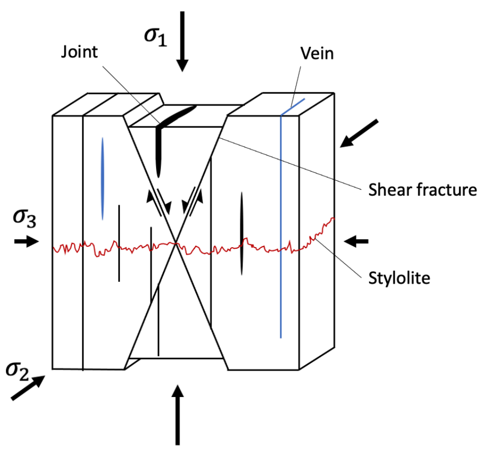

Figure 2.1: Diagram showing fractures concerning tree principal stresses (modified after Fossen 2010).

Mode I fractures form orthogonal to the fracture plane. These fractures open in the direction of minimal principal stress σ_3 (as shown in figure 2.1). If filled (cemented) we call them veins, otherwise, joints (figure 2.1). Shear or mode II fractures form oblique at an angle of less than 45°to the maximum principal stress σ_1, and demonstrate relative displacement parallel to the fracture plane (Kopf 2006). Often these fractures develop conjugate pairs (figure 2.1). Conjugate pairs are recognized as two sets of mode II fractures intersecting at 50°- 70°. In the field, they are identified by the presence of shear indicators, the intersection angle and/or striation on the fracture plane. Stylolites form irregular surfaces orthogonal to σ_1 (figure 2.1). They form as a result of pressure solution processes (Bruna et al. 2019). Stylolites, together with extensional and shear fractures play an important role as principal stress indicators (figure 2.1).

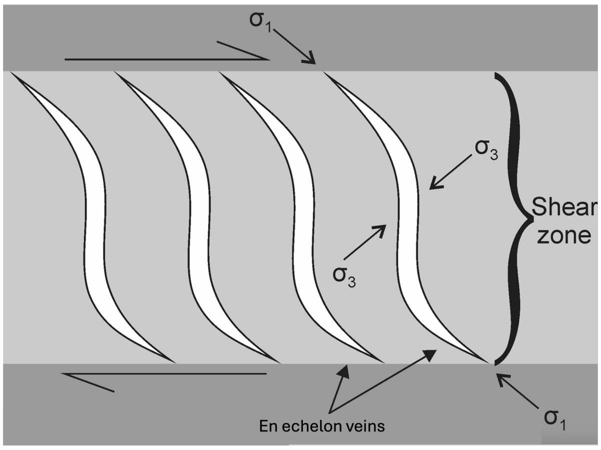

Figure 2.2: Diagram showing principal stress orientations regarding en echelon fractures, modified from Tóth et al. 2020.

Fractures that display both opening and shear characteristics are known as hybrid fractures or en echelon. These discontinuities form under mixed tensile and compressive stress at acute angles to the maximum principal compressive stress (Ramsey and Chester 2004, Bertotti et al. 2017). These discontinuities were abundant in the field (figure 2.3) and can also be used as stress indicators. En echelon fractures open in the direction of σ_3, and form at an angle to σ_1 (figure 2.2).

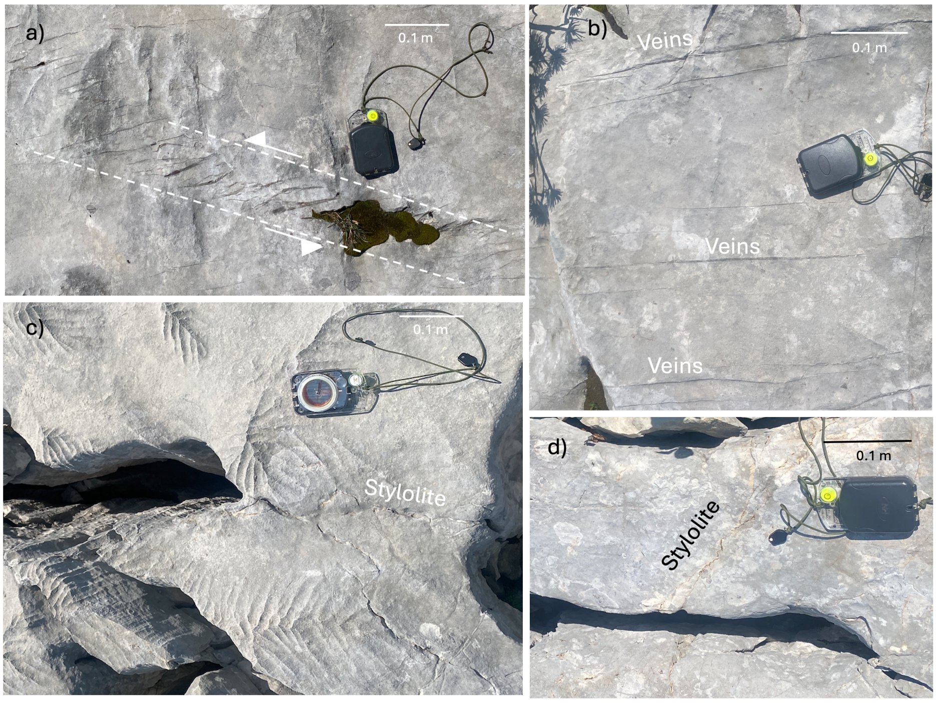

Figure 2.3: Diagram showing different discontinuities observed in the field: a) en echelon, b) veins (mode I), c) and d) stylolites.

In this report, we refer to lineaments when discussing linear structures traced on the Earth's surface, which represent brittle discontinuities, such as faults, fractures, stylolites, veins, en echelon veins, and karstified discontinuities.

2.1.1. Fracture Sets and Associations

Within a rock unit, fractures can be grouped in sets, based on shared similar orientations, fracture type, topology, relative age or kinematics (Sanderson et al. 2024). A single rock unit can often contain multiple fracture sets that form under different geological conditions or at different times. If different fracture sets are formed under the same stress field (same orientation of principle stress), we can group them into associations (figure 2.6). Fracture associations can indicate orientations of principal stresses, and therefore inform us about the tectonic history. Multiple associations present in a single rock unit indicate changes in the orientation of principal stresses. These changes can be either regional, such as tectonic (far-field) stresses and rock burial, or local, generated by faulting or folding. Local stress field alterations result in a spatially variable fracture network.

An example of fracture association is represented in figure 2.1, where we see orientations of three different types of discontinuities (mode I, mode II, and stylolite) related to the position of three principal stresses. This diagram represents one possible configuration in nature, but it is not always observed in practice. Usually, two sets of fractures are identified in the field or other data sets. Figure 2.4 shows associations of two discontinuity sets. All three configurations provide sufficient information to identify the orientation of each principal stress. In the case of a single fracture set present, it is still possible to determine all three principal stresses, however, it is not always reliable. If mode II fractures form a conjugate pair, we consider this as two different sets.

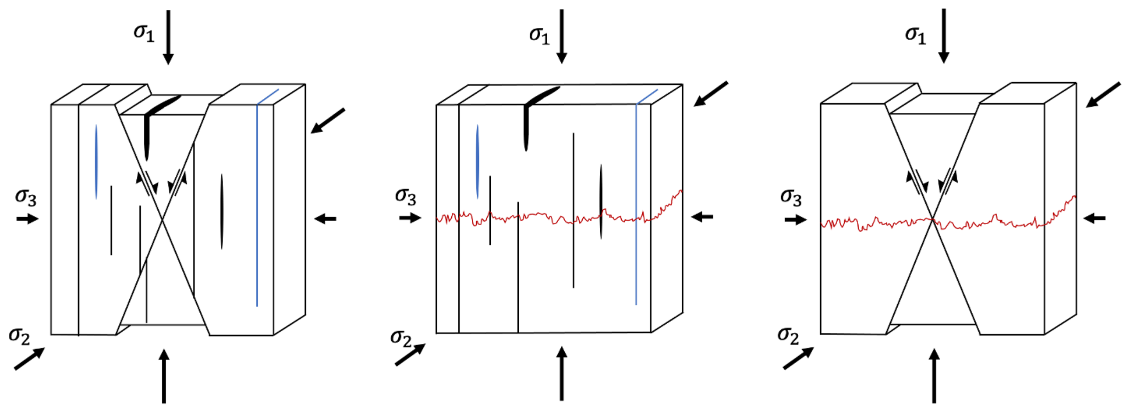

Figure 2.4: Possible discontinuity associations. Associations of two discontinuity sets: a) mode I and mode II fracture; b) mode I and stylolites; and c) mode II and stylolites.

In case of only mode I opening fractures or veins present, only σ_3 can be determined. Stylolites can indicate σ_1, whereas conjugate pairs (mode II), en echelon or single shear fracture set, can indicate the orientation of all three principal stresses (2.5).

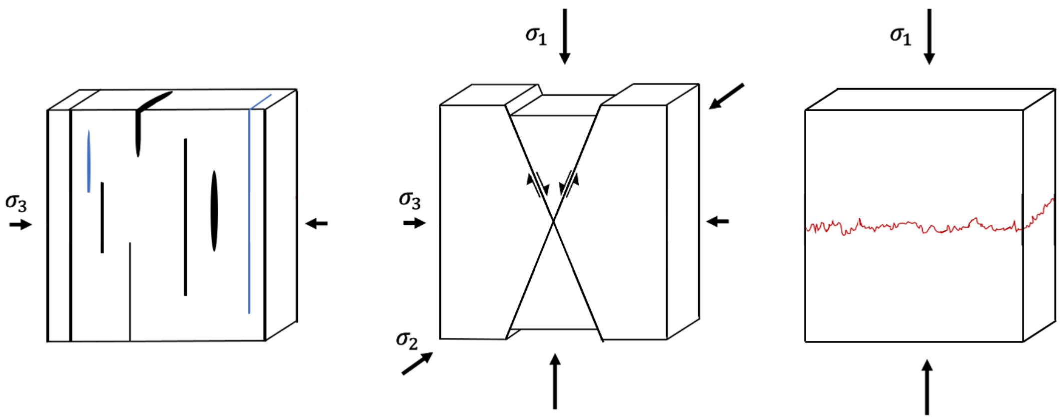

Figure 2.5: Possible discontinuity associations.

Term ”fracture association” is not commonly used in literature. Instead, fractures are grouped in sets, sets in deformation events, and events constitute a fracture network (Peacock et al. 2018). However, in this report, fracture sets are grouped in association, and fracture associations comprise a fracture network. This terminology is important as fracture, or more precisely, discontinuity associations can be used to indicate deformation events.

When interpreting deformation events (or stress regimes associated with fractures), considering fracture association rather than fracture sets helps simplify the network. Usually, one set is attributed to one event, which can make the fracture network complex and confusing. Fracture associations provide information on the directions of principal stresses, which are then used to interpret events.

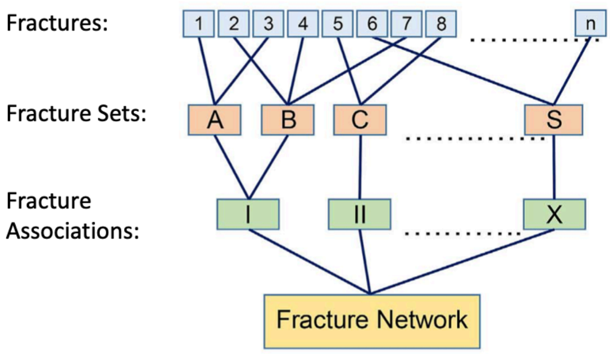

Figure 2.6: Fractures can be grouped into sets and sets into fracture associations (modified after Peacock et al. 2018 at the association level).

2.1.2. Topology

Topology is used to describe a fracture network as systems of branches and nodes (Sanderson and Nixon 2015). Branches are fracture traces and nodes represent the relationship between our traces. Three types of nodes are recognized: I-nodes (isolated fractures), Y-nodes (abutting) and X-nodes (crossing) (figure 2.7).

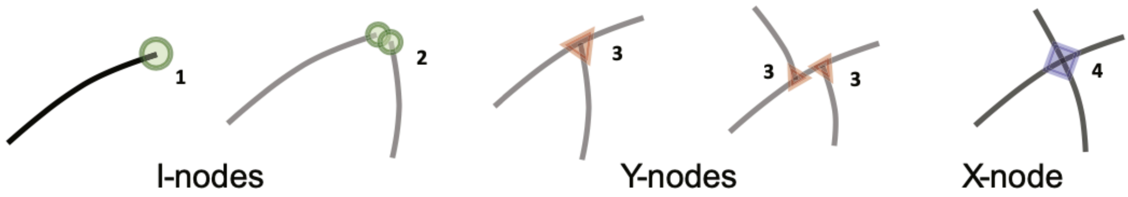

Figure 2.7: Different node types (Peacock et al. 2016).

To analyse topology FracPaQ plots the nodes on a ternary diagram (Manzocchi 2002). The plot shows the relative proportions of nodes in the fracture network. An example of the plot is shown in figure 2.8. Ternary plots can be used to distinguish different networks (Sanderson and Nixon 2015) and to determine if there are any trends in topology at different scales.

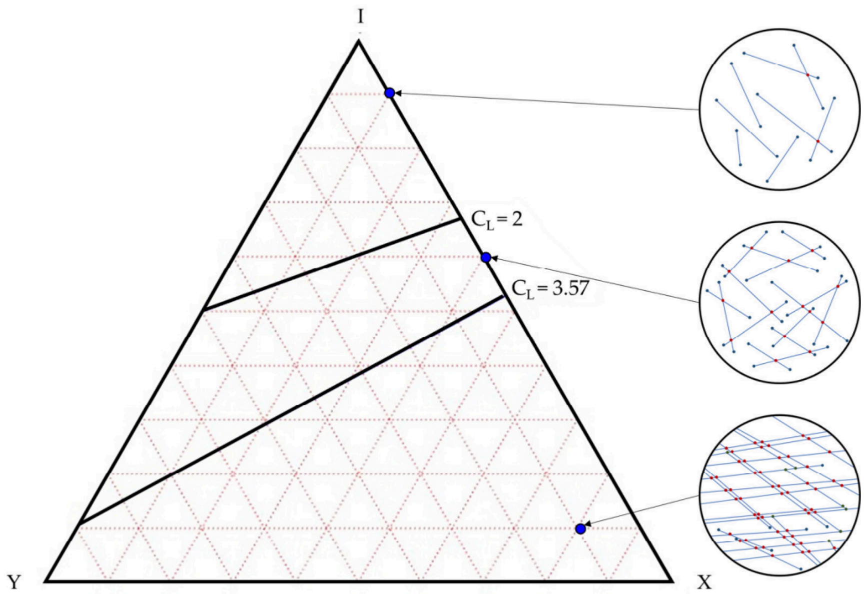

Figure 2.8: Example of the ternary plot of I–X–Y proportion. CL (contour line) represents the average number of connections per line (black solid lines). The three sets of traces that simulate fracture networks show how the fracture network topology is characterised using the I–X–Y parameters, from Ong and Jamaludin 2023.

3

Geological Setting

3.1. Present-day Situation

The Parmelan plateau is a flat-topped box-fold anticline located in the frontal part of the Bornes Massif - a fold-dominated thrust belt with NE–SW striking folds. It is situated in the northern Subalpine chains of the Dauphinois domain in southeastern France (Berio et al. 2021). The carbonate plateau is characterised by intense karstification, shaping the present-day landscape.

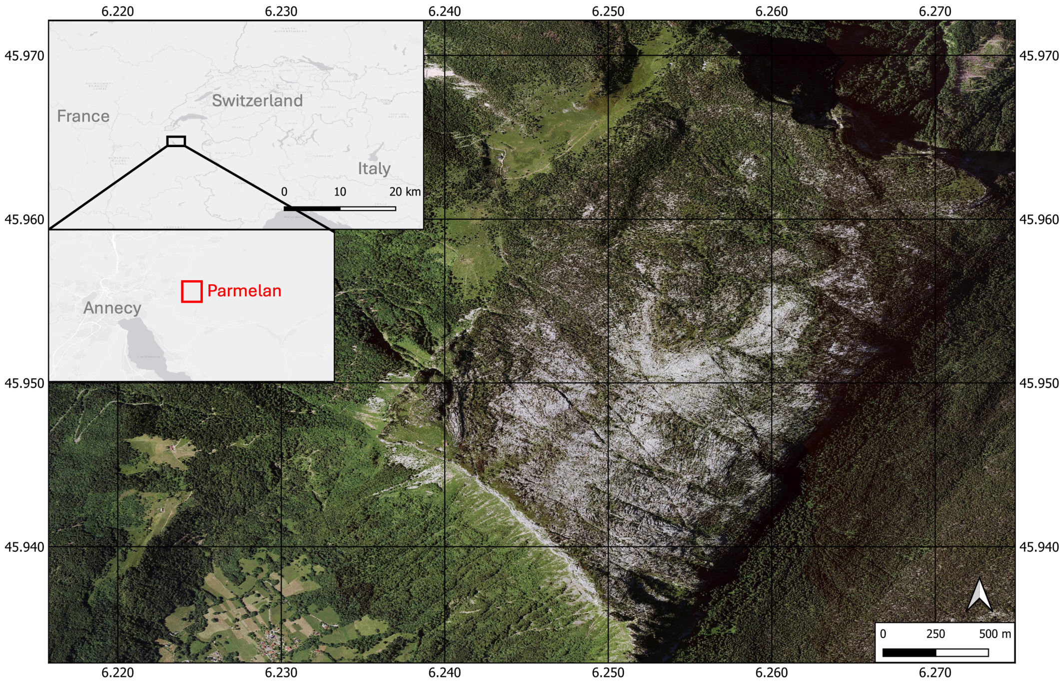

Figure 3.1: Satelite image of the Parmelan plateau, located 10km north-east from Annecy, France.

The NE-SW trending anticline has a 2km wide flat plateau and steep dipping limbs (Berio et al. 2018), exposing Urgonian Limestones with bedding surfaces dipping less than 10–15° in various directions. The forelimb of the Parmelan anticline dips at 50–60°toward the northwest. The backlimb shows progressively increasing bedding dip angles, reaching 60–70°(Berio et al. 2021).

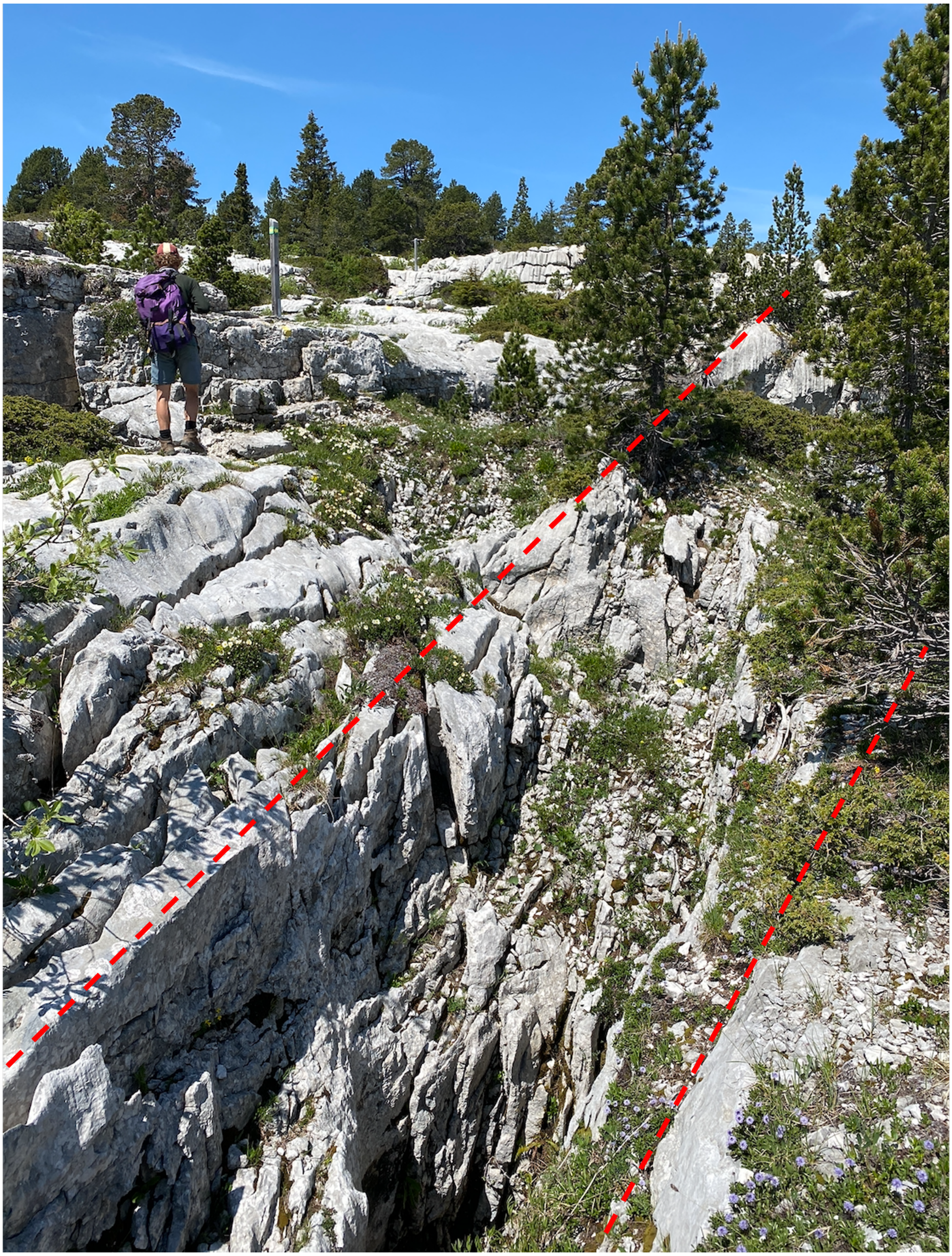

Figure 3.2: Example of one of the fracture corridors from the field.

3.1.1. Structural Context

According to Berio et al. 2021, the anticline includes a pre-folding extensional fault that trends parallel to the fold axis (figure 3.4). In addition to box-fold geometry, the Parmelan demonstrates structural features visible on satellite images, striking NW-SE and roughly E-W (figure 3.1). These discontinuities have been described as transversal faults by Berio et al. 2021, and riedel faults by Lismonde 1983a. It is also hypothesized that they could be fracture corridors (figure 3.2).

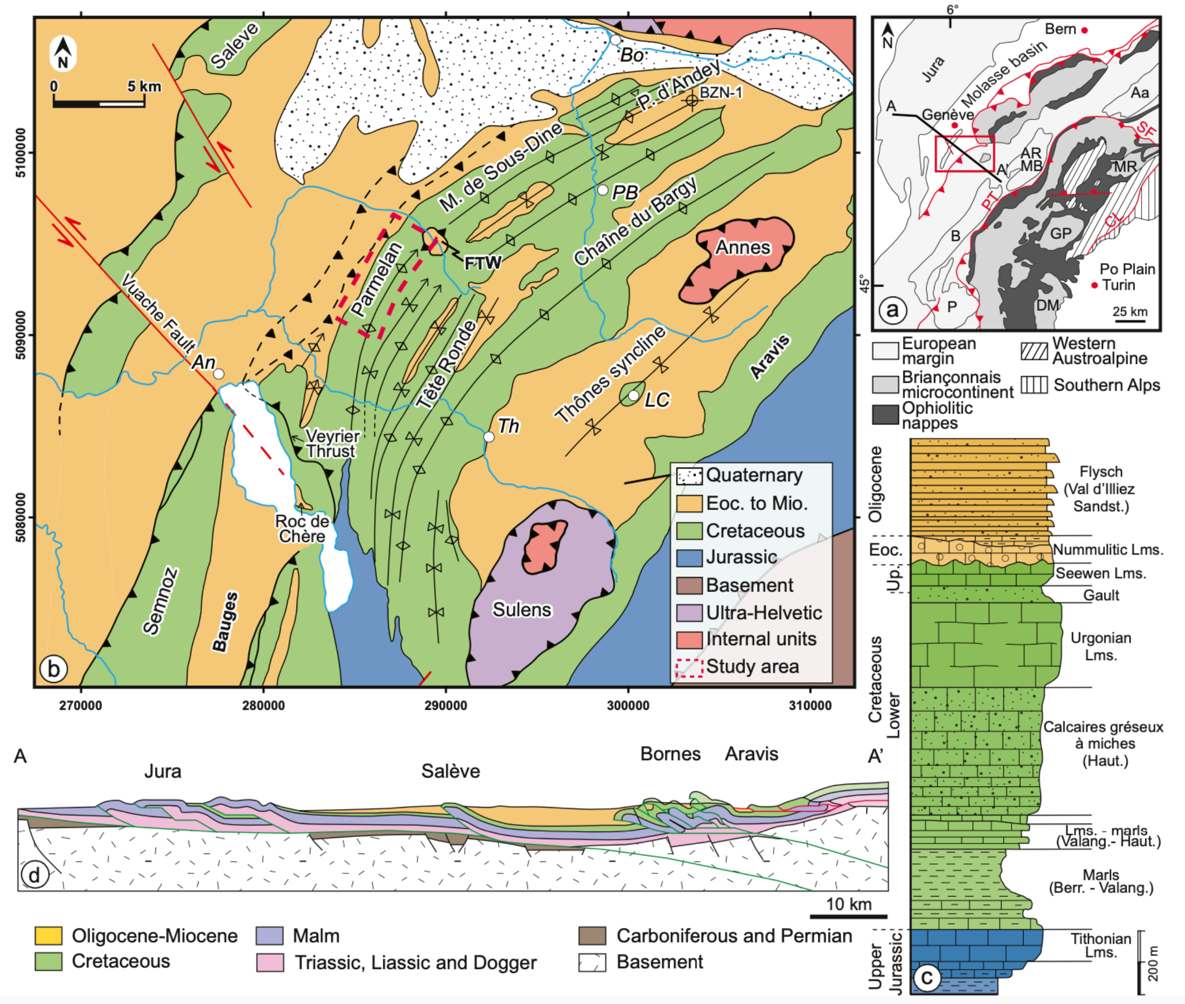

Figure 3.3: Geological and structural map of the Bornes Massif, from Berio et al. 2021.

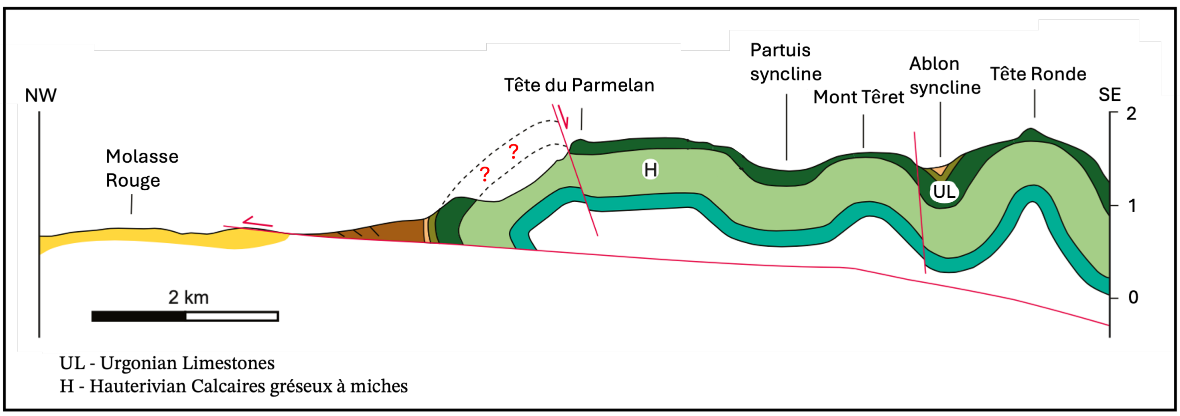

Figure 3.4: NW-SE geologic cross-section through the Tête Ronde, Mont Téret and Parmelan anticlines, modified after Berio et al. 2021.

3.1.2. Karst

Karst is a dominant feature of the Parmelan Plateau. Lismonde 1983b introduces karst at the Parmelan as lapiaz (or lapies) which referes to a weathered limestone surface found in karst regions and consisting of etched, fluted, and pitted rock pinnacles separated by deep grooves. This rugged surface is formed by the dissolution of rock along discontinuities (fractures, faults...) and other heterogeneities, by water containing carbonic and humic acids (Blatnik et al. 2020). In the case of Parmelan, this happened due to meteoric precipitation, which causes the rock to dissolve.

Many different karst features are recognized at Parmelan. However, the most relevant for this study are sharp peaks (figure 3.6 a)) formed on initially smooth horizontal surfaces or slightly inclined surfaces (Blatnik et al. 2020), and rinnenkarren (grooves) - solution channels (runnels, flutes) that run down the dip of a slope (Veress 2009). The peaks are shown in figure 3.5 where the shape of karst depends on the inclination of the surfaces. Figure 3.6 b) shows an example of rinnenkarren from the field. Both of these features are visible on UAV images.

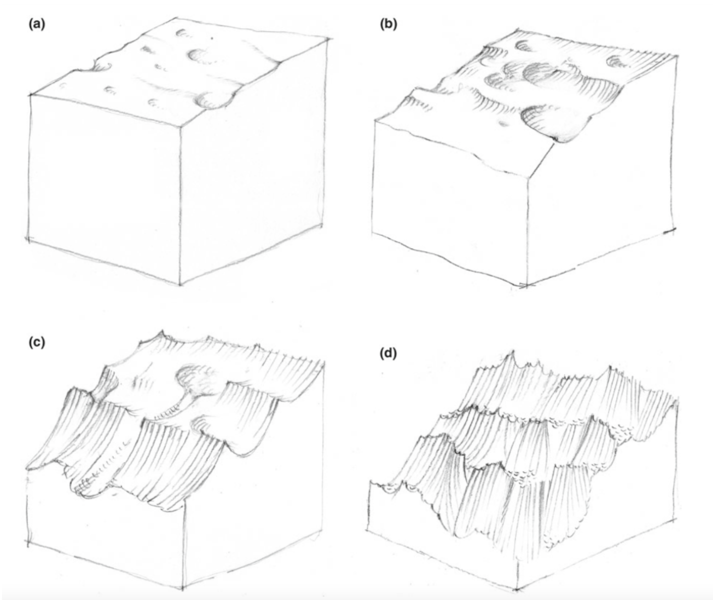

Figure 3.5: Developing model of the slightly inclined surface of the rock, from Blatnik et al. 2020.

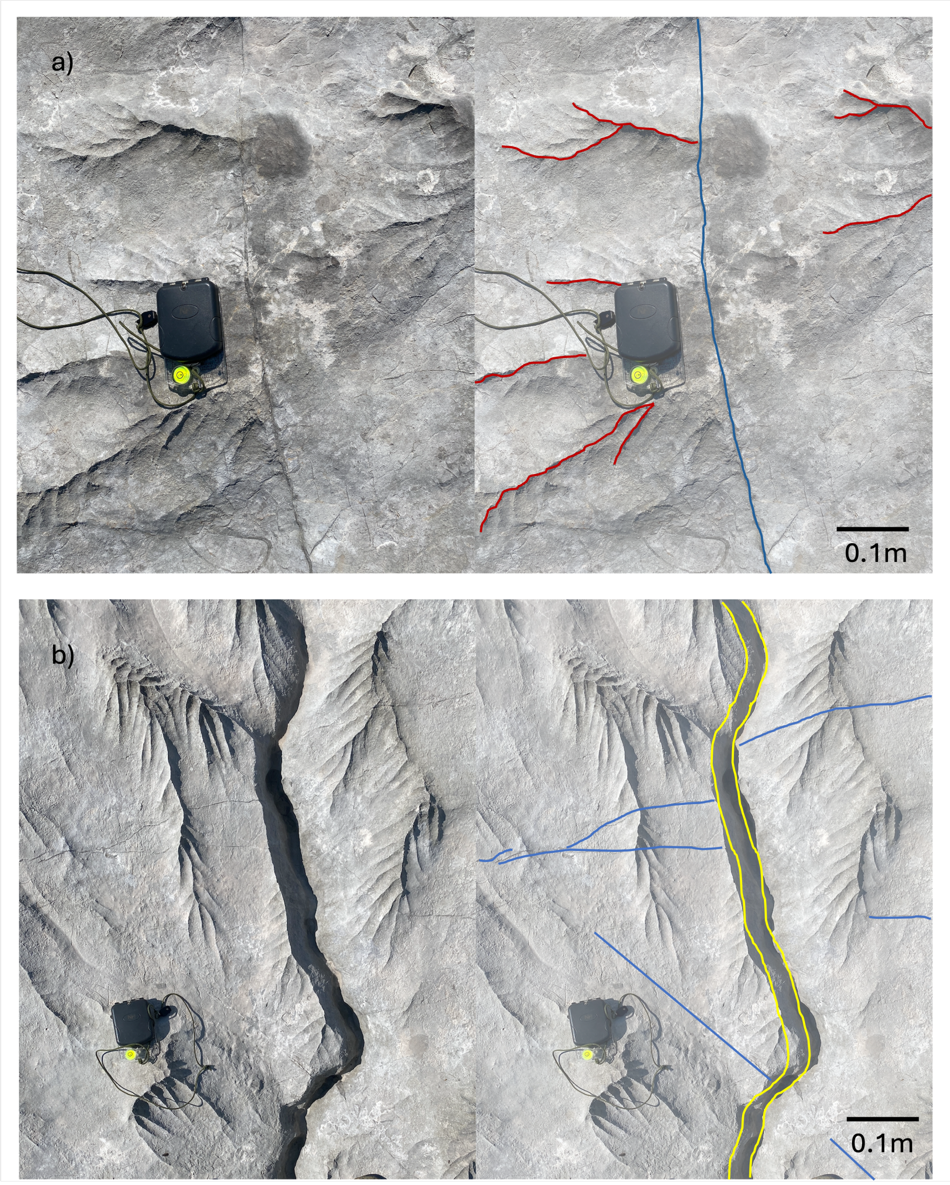

Figure 3.6: Example of a) sharp peaks and b) rinnenkarren taken in the field. Peaks are marked in red, rinnenkarren with yellow, and veins are in blue.

3.2. Geological History

The Parmelan anticline has gained attention due to its exceptional outcropping conditions, which allow us to investigate its structural complexity. The geological history of the Parmelan Plateau begins with the deposition of marine sediments during the Mesozoic era, specifically the Cretaceous period. The dominant sedimentary formations include the Urgonian Limestones, deposited during the Late Hauterivian to Early Aptian stages. These limestones are characteristic of shallow marine environments and carbonate platforms.

Initial sedimentation occurred in a relatively stable tectonic setting. In the Late Cretaceous the tectonic activity increased, leading to the formation of early folds and faults. This period marked the onset of the Alpine orogeny, which significantly influenced the region's geology (Berio et al. 2021). The collision between the European and Adriatic continental margins (Dal Piaz et al. 2003) and therefore the closure of the Tethys Ocean, causing widespread deformation. This tectonic activity resulted in the complex folding and faulting observed in the Parmelan Plateau. The compression during this period led to the uplift of the region and the development of the plateau's distinctive flat-topped box-fold geometry.

The forelimb of the Parmelan anticline dips steeply towards the northwest, while the backlimb shows progressively increasing bedding dip angles, becoming locally overturned. This suggests a significant amount of tectonic shortening and folding.

Following the main phases of the Alpine orogeny, the region experienced erosion and weathering, which further sculpted the landscape of the Parmelan Plateau. The present-day topography reflects the combined effects of tectonic uplift, folding, faulting, and subsequent erosion and karstification.

3.3. Geothermal Potential

The Urgonian limestones, along with other Lower Cretaceous units, act as a significant regional aquifer (Clerc et al. 2015). The aquifer potential is enhanced by the karstified nature of the limestone, with evidence from various wells indicating substantial flow rates (Clerc et al. 2015). For instance, geothermal well GEo-01, drilled in 2018, report a flowrate of 50 l/s of geothermal water at 34°for this unit (Moscariello 2019).

The Lower Cretaceous units exhibit low primary properties, with porosity less than 8% and permeability ranging between 0.001 and 10 mD (Moscariello 2019). Despite this, secondary porosity and permeability associated with fractures and karst features provide the necessary conditions for an effective reservoir.

Fracture and karst networks in the Mesozoic sequence are important for ensuring good reservoir properties, and storage capacity, although their connectivity is equally important for providing sufficient permeability to the geothermal system.

Karstification is a key geological process in the Parmelan region, affecting the reservoir characteristics of the Urgonian limestone formation. The karstification extends into the underlying Pierre-Châtel Formation (Rusillon 2017), indicating a substantial vertical extent of karst processes.

The presence of siderolithic sandstone infill within the karst features, identified in wells (such as Thônex-1), suggests episodes of low permeability due to plugging of the main open fractures and karsts (Clerc et al. 2015). Despite this, the karstified zones can still offer significant hydrogeological benefits, as evidenced by thermal water exploitation in Divonne-les-Bains, which produces high flow rates from shallow depths (PGG 2011).

However, the spatial distribution of karst and the characteristics of the sedimentary infill remain uncertain and are subjects of ongoing geophysical studies.

4 Methods

Airborn and field survey data of the Parmelan plateau were analyzed and interpreted. This chapter outlines already available data, the fieldwork done to collect the data and the methods used to characterize the data.

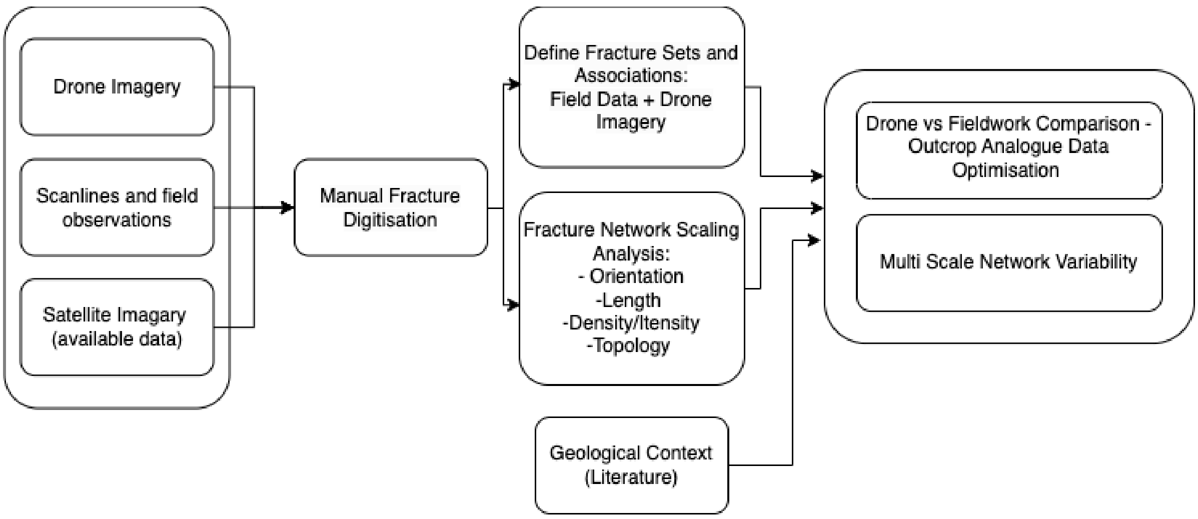

Figure 4.1: Project workflow.

4.1. Fieldwork

Outcrop analogue data provides valuable information for studying natural fracture networks in a rock formation, as it allows for the direct observation of the fractures in their natural setting. Fieldwork allows us to gather detailed information about the spatial distribution and topological relationships of the fractures — data that is impossible to observe from the subsurface data alone. While it is challenging, retrieving partial subsurface data and predicting the fracture geometry is possible.

To gain a better understanding of the study area and validate already available UAV images, 2-week geological fieldwork was conducted at the Parmelan (France) in June 2023, together with PhD candidate Jasper Hupkes. Structural data was collected for the duration of the trip. This includes fracture types, fracture orientations, spacing, length and aperture. Furthermore, additional high-resolution drone images of the exposed rocks have been taken.

4.1.1. Linear scanlines

Linear scanline is a fracture data collection method where a physical (or virtual) line is placed on the outcrop and fracture parameters are collected at every fracture intersection point (Martinelli et al. 2020). Three scanlines have been recorded in the field (table 4.1), at three different stations (figure 4.2). The locations have been chosen based on the accessibility of the pavement and vegetation or debris cover. Additionally, we chose locations suitable for taking high-resolution UAV images as the goal was to combine (and compare) these two data sets.

In this report, we refer to field scanlines to data that was recorded in the field. Virtual scanlines refer to lines drawn in QGIS, at the same location (explained later).

Table 4.1: Scanlines are named after the stations. Discontunieties include fractures, veins, and linear karst formations (sinkholes, rinnenkarren not recorded).

Station	Scanline	Length [cm]	Orientation (Strike)	Number of discontinuities	Of which Karst
Station 1	Field Scanline 1	2880	170	48	4
Station 2	Field Scanline 2	2085	002	40	3
Station 3	Field Scanline 3	2515	150	49	22

Scanline data recorded in the field includes: the position of discontinuities (fractures, veins, stylolites) and karst (on the line), orientation (strike) and length. The length has been grouped into three categories: S (short discontinuities where length l is less than $1m$), M (medium, $1m < l < 5m$) and L (long, $l > 5m$). This is done to increase the speed of data acquisition. Additionally, it also minimises the censoring bias as all fractures longer than $5m$ are considered an ”L” fracture. Censoring occurs when fractures that are partially visible or too small to be recorded are excluded from the data set, leading to an underestimation of the actual fracture lengths. Fracture length criteria for ”S” and ”M” were set based on field observation, aiming to set representative numbers.

Karst features that were assumed to be dissolved fractures/veins were recorded on the scanlines. Sinkholes, rinnenkarren and sharp inclined karst surfaces have not been recorded. The scanlines were positioned perpendicular to the most abundant fracture set to minimize the orientation bias.

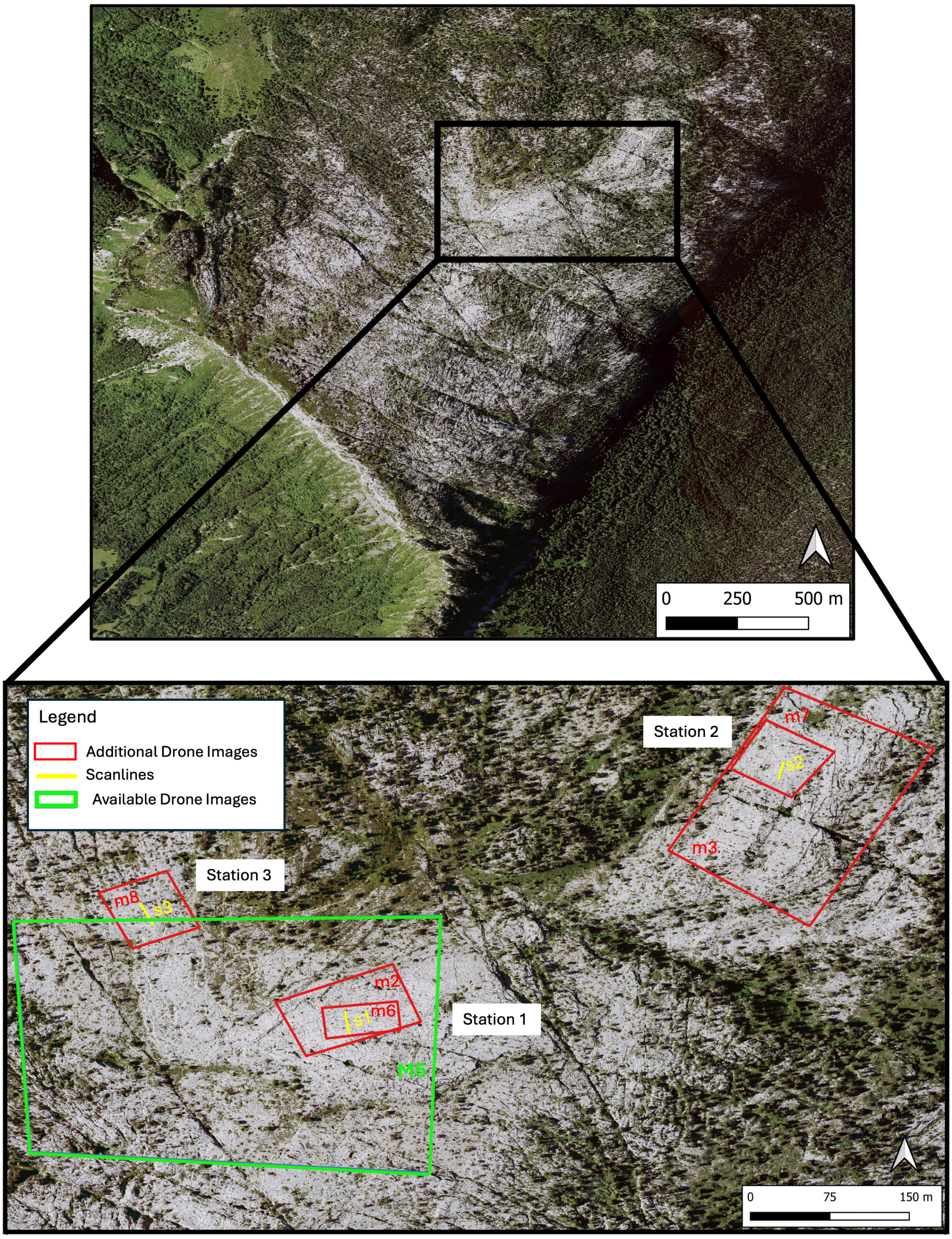

Figure 4.2: Study area is shown in this map. Three stations are marked on the map, including three scanlines (in yellow - named after the stations), additional drone images talked in the field (in red), and drone images already available (in blue).

4.1.2. UAV and Satellite Data

Images of fractured outcrops collected using unmanned aerial vehicles (UAVs) are becoming more accessible and cheaper to obtain. UAVs can capture high-resolution images from centimetre to kilometre scale. Some UAV imagery data was already available (at lower resolution) for the Parmelan plateau, and the rest was taken in the field (figure 4.2). Data was captured using the DJI Phantom 4 drone.

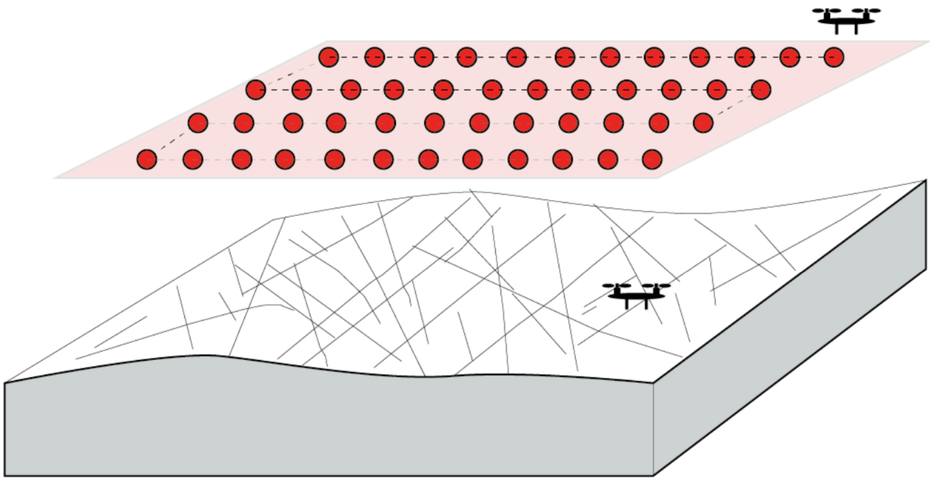

Figure 4.3: UAV planned mission above the pavement: following a pre-programmed route (from Steijn 2018).

The Pix4D Capture App was used to design the flight path (figure 4.3). The user specifies the area to be covered, the flight altitude, and the overlap of adjacent images. The altitude determines the resolution of the captured images, lower altitudes generate higher-resolution images (in cm/pix), which are essential for detailed analyses. For instance, high-resolution images were captured at a $10m$ altitude (missions m6 and m7, Table 4.2), allowing for a detailed interpretation of pavement fractures. However, in some locations, high vegetation required a higher flight altitude. For example, mission m8 was conducted at a 15m altitude, resulting in lower-resolution images. We lose 50% of resolution by flying at $15m$ high compared to $10m$ high (table 4.2).

The flight time for each mission depends on the area to be covered, the altitude, and the image overlap. After the flights, the collected images are processed using Agisoft Photoscan Professional software to create high-quality pavement orthomosaics. These orthomosaics are stitched together from the individual images, providing a detailed pavement view.

Table 4.2: Flight mission information. Note that for mission m6 the data is not complete due to battery shortage, and M5 is already available drone data.

Mission	Altitude (m)	Overlap (%)	Resolution (cm/pix)	Extend (wxh)	Flytime (min)
m2	20	80	0.88	98x74	8
m3	46	80	2.0	231x126	8
m6	10	80	0.44	N/A	N/A
m7	10	80	0.44	63x69	14
m8	15	80	0.66	58x71	7.3
M5	NDA	NDA	2.0	NDA	NDA

UAV images of the pavements have been manually and automatically traced, using QGIS software and the method developed by Prabhakaran et al. 2019, respectively. The automated method traces fractures using a complex shearlet transform coupled with post-processing algorithms (Prabhakaran et al. 2019). Unfortunately, this tracing method produced unsatisfactory results due to high noise levels. Any signal that is not generated by a geological fracture is considered noise. The method picks up karst features that are not necessarily aligned with fractures (sinkholes, rinnenkaren, ect...), vegetation and shadows. Therefore all the pavements have been interpreted manually, explained in the following section.

4.2. Fracture Network Digitisation

High-resolution orthomosaic images (m6, m7 and m8) have been interpreted at 1:10 scale. The remaining images (m2, m3 and M5) have been traced at 1:250 and 1:500, and the satellite image has been traced at 1:1000 and 1:7000.

Table 4.3: Fracture digitisation scale information.

Mission	Digitisation Scale	Area $[m^2]$
m2	at 1:250 & 1:500	4.800
m3	at 1:250 & 1:500	12.000
m6	at 1:10	1.200
m7	at 1:10	1.200
m8	at 1:10 & 1:250 & 1:500	3.015
M5	at 1:250 & 1:500	63.000
Satellite	at 1:1000 & 1:7000	4.000.000

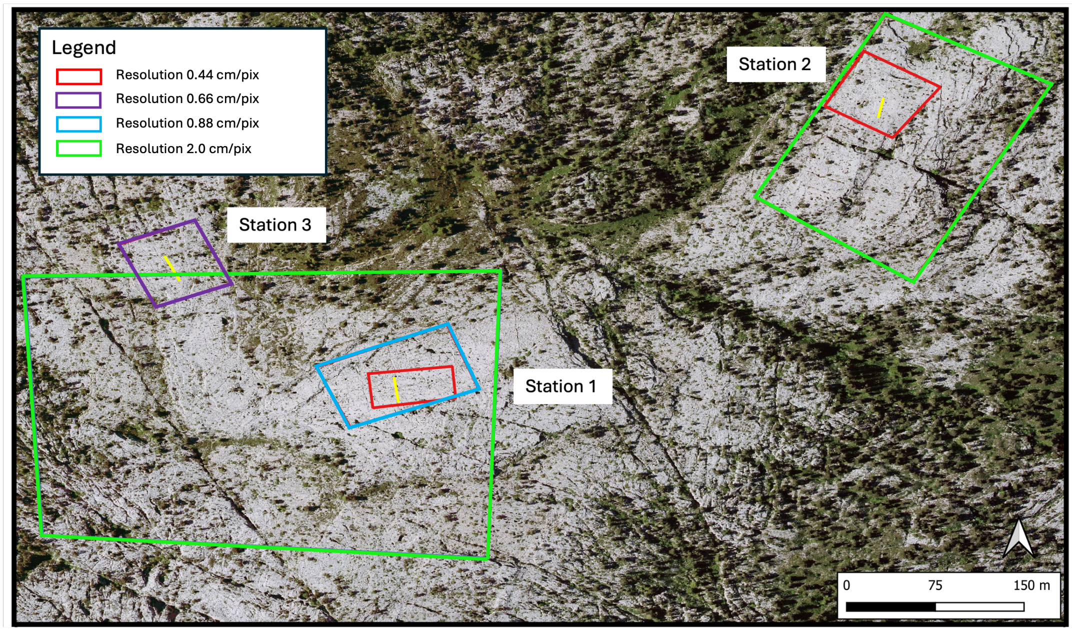

Figure 4.4: Resolution of each image used to trace discontinuities.

When interpreting manually:

- We consider the scale (or the zoom) at which the fractures are traced. Discontinuities on the pavements have been traced at various scales, meaning different levels of zoom were used to capture these features. We start by zooming out until only large-scale discontinuities are visible on the pavement. For the Parmelan plateau, this was determined to be at 1:7000, on the satellite image. After determining this large-scale view, we then select the next scale by zooming in until additional, smaller discontinuities become visible and distinct. Fractures have been interpreted at the following scales: 1:7000 and 1:1000 - satellite scale, 1:500 and 1:250 - UAV scale. Furthermore, high-resolution images were interpreted at a 1:10 scale, which was the highest possible zoom before the images got too pixelated.
- Next, we considered the area. We choose areas not covered in debris and vegetation; preferably less eroded areas (less rock debris); and ideally clear exposure.
- Lastly, it is essential to establish clear guidelines for the tracing process when interpreting manually. It is important to set clear rules so that the interpretations can be recreated. For Parmelan we use the following rules:

1. Discontinuities are traced from tip to tip.
2. Only linear discontinuities are traced (fractures that follow a straight line path or nearly straight line path), to avoid confusion with karst features.
3. Fractures are traced across sinkholes if the distance between the tips is $< 1m$ (use measuring tool in QGIS) for 1:10 zoom; $< 2m$ for 1:250; $< 3.5m$ for 1:500; $< 7m$ for 1:1000; and $< 50m$ for 1:7000 - and if the fracture on each side of the karst feature follows the same straight line path. This is also applied to patches of soil or vegetation.
4. Due to the similar colour of the vein cement and the host rock, the previous rule applies also to the veins that stop being visible on the image and appear again. Besides the colour of the cement, this can also be due to the resolution of the image, the amount of light (weather conditions) when the image was taken.
5. On a large scale, where fractures are highly karsified, we trace in the middle of two fracture walls.
6. Minimal fracture length was set for each scale: for 1:10 zoom no minimal length; $L_{min} = 3m$ for 1:250; $L_{min} = 15m$ for 1:500; $L_{min} = 75m$ for 1:1000; and $L_{min} = 250m$ for 1:7000. This is done as the resolution becomes more limiting as we zoom out (Prabhakaran et al. 2019).
7. En echelon veins are visible on high-resolution images, and they're traced across the middle of propagation direction (see example figure 4.6).

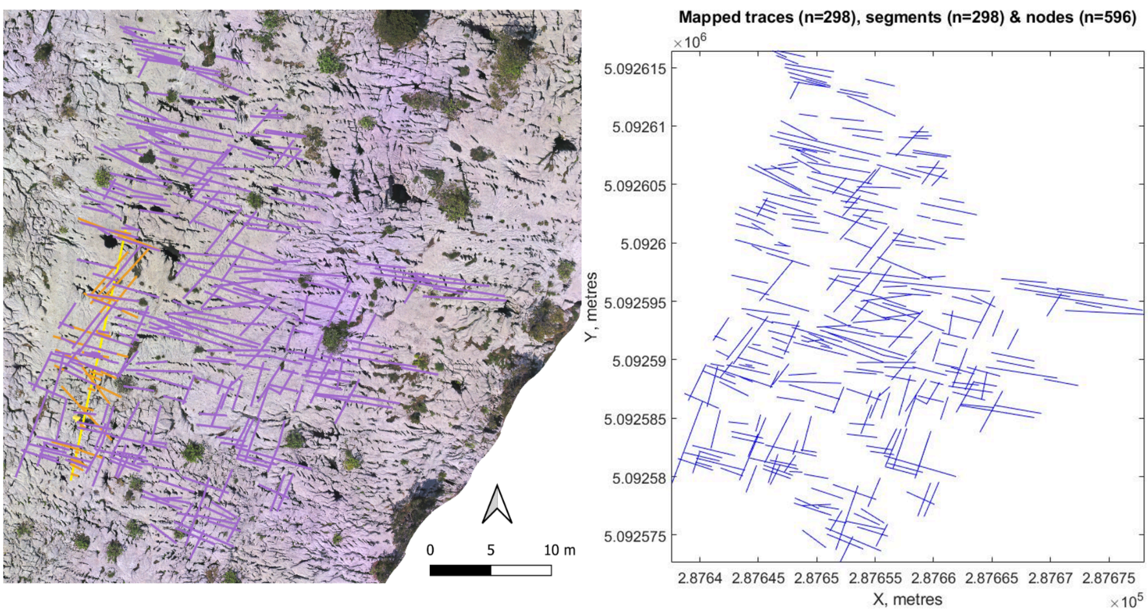

Figure 4.5: Manually traced image at 1:10 (mission m7).

Parmelan is a highly karstified outcrop, with karst features visible on every scale. Only at field scales (1:10) fractures (mode I and II), stylolites and en echelon are visible. At higher scales (1:250, 1:500, 1:1000 and 1:7000) these discontinuities are karstified. Fracture networks at higher scales could be considered karst networks.

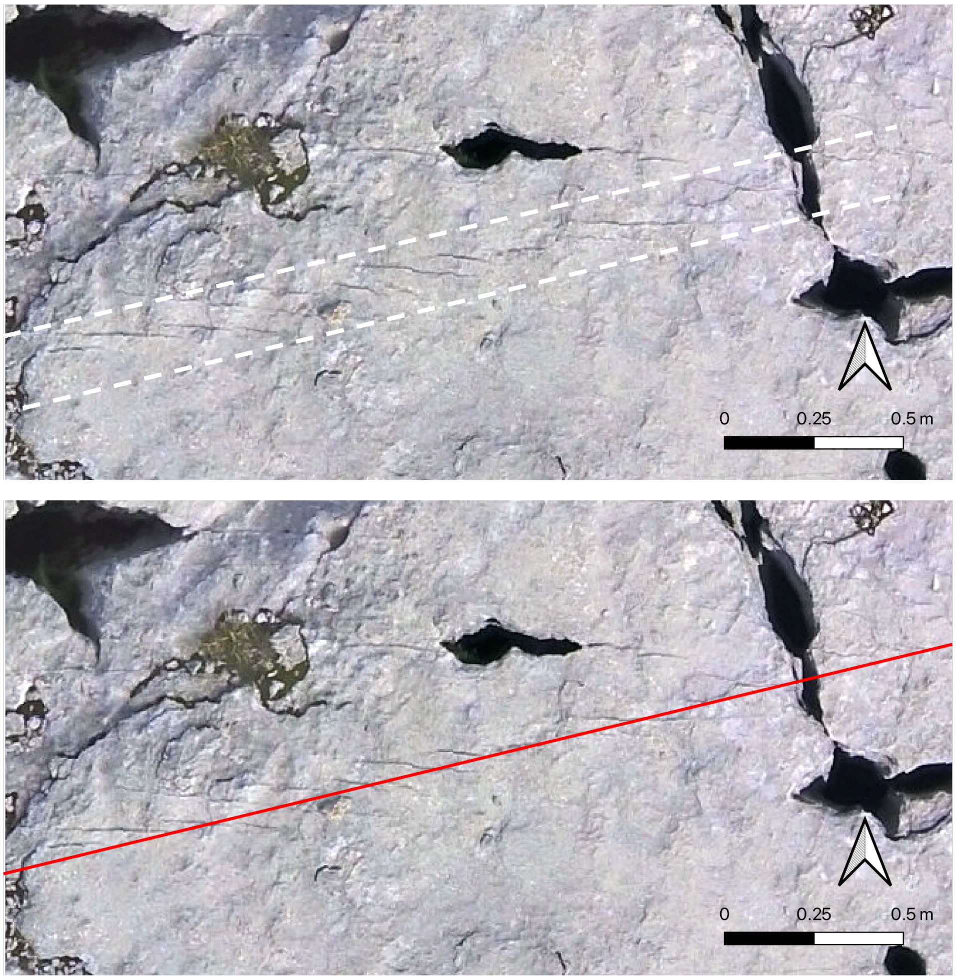

Figure 4.6: Example of tracing en echelon veins visible on drone images.

Besides orientation bias and censoring, this data collection method also encounters truncation and size bias (Zeeb et al. 2013). Truncation bias is caused by resolution limitations depending on the detection device used. At certain scales, rock discontinuities are not visible anymore (Zeeb et al. 2013). Size bias is related to the fracture length - shorter fractures have less probability of intersecting the scanline and are usually undersampled (Martinelli et al. 2020).

4.2.1. Fracture Tracing Corrections

To make sure that intersections between fractures (the nodes) are accurate, a manual snapping tool in QGIS 3.34 was used to correct the intersection points at each scale. This was done where gaps or overlaps are present (figure 4.7). By applying this correction we ensure that the Y nodes are also well represented.

From this 2D fracture trace maps have been created (example fig. 4.5). These maps contain information on the geometry and topology of fracture networks (Prabhakaran et al. 2021), and can further be analysed after applying the graph theory (Sanderson et al. 2019, Manzocchi 2002).

Additionally, virtual scanlines were added on top of field scanlines. Virtual Scanline 1 is located at Station 1 (on top of Field Scanline 1), and so on... Virtual Scanlines intersect manually traced fracture network maps and are used to compare field and airborne fracture data collection techniques.

Finally, the data (2D fracture maps) has been exported and converted into a text file, then imported into the FracPaQ software for further analysis. With the software traced data can be quantified, which makes fracture classification possible. Furthermore, an analysis of fracture length, orientation, intensity, density and topology has been conducted, further explained in the following sections.

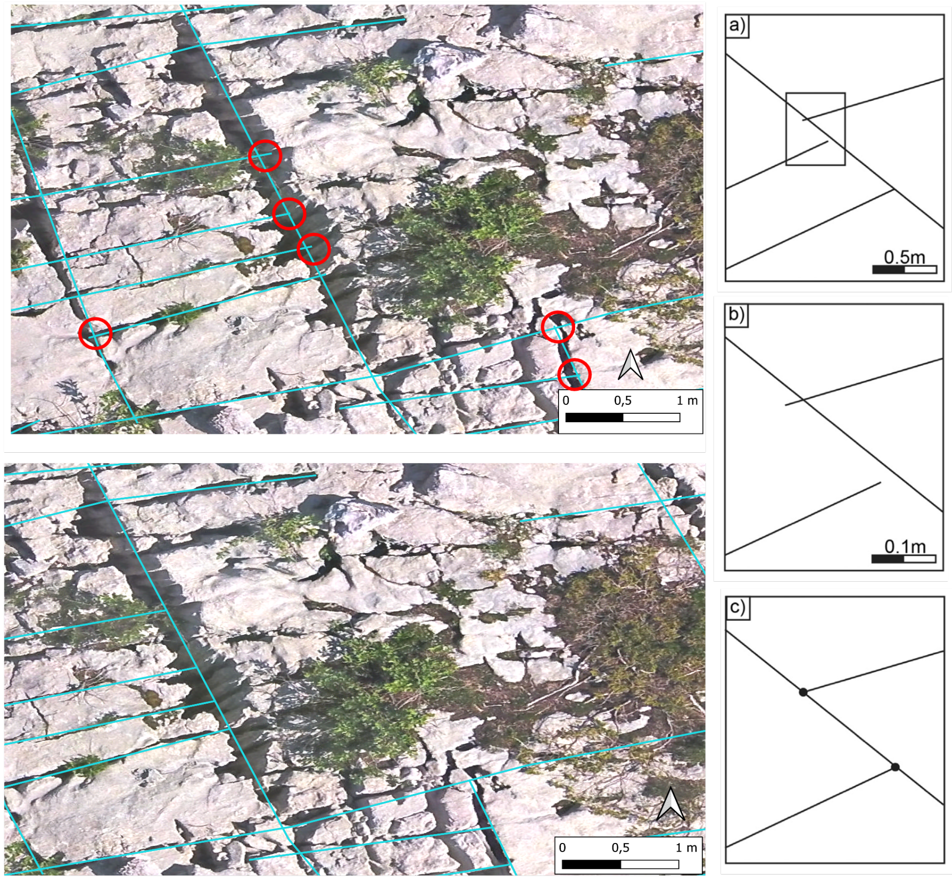

Figure 4.7: Example of fracture tracing correction using the manual snapping tool. Diagram (right) from Bisdom et al. 2017

4.2.2. FracPaQ: Fracture Network Analysis

FracPaQ software is a Matlab package that automatically analyzes traced fractures and outputs the relevant geometry parameters (Healy et al. 2017). The parameters analysed in FracPaq are the following: orientation, length, and connectivity (topology).

4.2.3. Trace length and Orientation

To compare length on multiple scales, the data was fitted with power-law, lognormal and exponential fits. From here the best-fit distribution was determined and compared on different scales. It is important to keep in mind that trance length is affected by censoring because some discontinuities are not fully visible (Mauldon et al. 2001). Length bias is also present, as it is more likely to pick longer than shorter fractures (Mauldon et al. 2001).

FraqPaQ plot trace orientation on rose diagrams. Network orientation data was analysed and compared on multiple scales. Additionally, trace length and orientation of high-resolution data was also compared to the field data.

4.3. Density and Intensity

For scanline measurements P10 - parameter representing fractures per unit length of scanline - was used:

$$P_{10} = \frac{N_f}{L}$$

where N_f is the total number of fractures intersecting the scanline, and L is the length of the scanline.

Fracture network density is defined as the number of fractures (traced lineaments) per unit sampling area - P20.

$$P_{20} = \frac{N_f}{A}$$

where:

- P_{20} is the fracture density parameter.
- N_f is the number of fractures (lineaments).
- A is the area over which the fractures are counted.

Intensity is the length of fracture traces per unit sampling area - P21 (Mauldon et al. 2001).

$$P_{21} = \frac{\sum_{i=1}^{N} L_i}{A}$$

where:

- P_{21} is the fracture intensity parameter.
- $\sum_{i=1}^{N} L_i$ is the total trace length of all lineaments.
- A is the area over which the lineaments are counted.

4.4. Classification Fractures into Sets and Associations

Mode I and II fractures, stylolites and en echelon veins are (to a certain extent) visible in high-resolution images (missions m6 and m7). Recognizing and tracing these discontinuities allows us to group fractures in sets and further in associations. This is only possible at the smallest scale (zoom level 1:10), whereas only karst networks were traced at higher scales. Due to high karstification levels and erosion, it is not possible to determine if the discontinuity traced is mode I, mode II, stylolites or hybrid fracture at higher scales. Therefore it is difficult to group these networks in sets and associations based on fracture type. These discontinuities could be grouped in sets based on their orientation, however with high uncertainties.

Fractures have been classified in sets based on: fracture type, orientation and cement. Furthermore, where the range of orientation is larger, Fisher's K value has been used. The Fisher K value describes the tightness or dispersion of an orientation cluster. The value ranges from 0 to 1, where 0 implies a more dispersed cluster (indicating possible multiple sets), and higher values imply a tighter cluster. The higher the Fisher K value the more likely it is that there is only one set present. After grouping fractures in sets, sets are grouped in associations based on the mutual relationships of these sets.

The Fisher's K value is given by the formula:

$$k = \sqrt{\left(\overline{\cos(2\theta)}\right)^2 + \left(\overline{\sin(2\theta)}\right)^2}$$

where:

- θ represents the fracture orientations in radians.

- $\overline{\cos(2\theta)}$ is the mean value of $\cos(2\theta)$.
- $\overline{\sin(2\theta)}$ is the mean value of $\sin(2\theta)$.

Field book notes and scanline data were used to characterize the fracture networks at a smaller scale to guide the interpretation of the fractures.

5 Results

5.1. Lineament Interpretation

Manual drone image tracing resulted in a total of 1771 lineaments, in total on all the pavements and at different resolutions. Small-scale interpretations (1:10) were used for the fieldwork vs UAV analysis. For the multi-scale analysis, all interpretations listed in table 5.1 were used.

Table 5.1: Sumarry of lineament interpretation.

Location	Mission	Scale	Spatial Coverage [m^2]	Number of Lineaments
Station 1&3	M5	1:500	51500	143
Station 1&3	M5	1:250	51500	341
Station 1	m6	1:10	1485	252
Station 2	m3	1:500	30450	44
Station 2	m3	1:250	12700	195
Station 2	m7	1:10	1400	302
Station 3	m8	1:10	2925	190
Parmelan	Satellite	1:7000	4000000	285
Parmelan	Satellite	1:1000	4000000	19

5.2. Fracture Network Analysis: Fieldwork vs UAV

Fracture network analysis at the outcrop scale (cm scale) was studied at three different stations (figure 5.1). At each station, linear scanline measurements (orientation, length and type of discontinuity) were recorded, including qualitative field observations (e.g. descriptive assessment of cement colour, structural features, etc.) and high-resolution drone images of the area. No lithological differences have been observed or recorded in the field between the stations. In this section field data is compared to data obtained using virtual scanlines.

Three study stations are shown in figure 5.1. Fracture orientation and length were studied and compared, furthermore, fracture associations were defined (UAV data).

5.2.1. Orientation Analysis

To compare fracture orientation measured in the field and traced on drone images, rose diagrams and stereonets were plotted for field and virtual scanlines.

When comparing the two sets of scanlines (field and virtual), a number of discontinuities are 'missing' from the virtual scanline. Virtual Scaniline 1 had 37% less lineaments traced (compared to Field Scanline 1), Virtual Scanline 2 had 37.5% less (compared to Field Scanline 2) and Virtual Scanline 3 had 55% less (compared to Field Scanline 3) (table 5.2). To illustrate this stereonets and barcode graphs were plotted for all the scanlines (figure 5.2). Barcodes are visual representations of P10 (number of fractures per unit of scanline length). Barcode data show a similar clustering pattern between field and virtual scanlines (figure 5.2). However, if we compare the stereonet data, there are a few NW-SE-oriented discontinuities that are not present on virtual scanlines 1 and 2, unlike in the corresponding field scanlines. Similarly, NE-SW-oriented discontinuities are missing in virtual scanline 3 compared to field scanline 3 (figure 5.2). This discrepancy raises the question of why these particular fracture sets are 'missing' in the analysis based on drone imagery.

Table 5.2: Number of discontinuities measured in the field (field scanlines) and traced on drone images

	Number of Discontinuities	Scanline Length [m]	P10
Field Scanline 1	46	29	1.59
Virtual Scanline 1	29	29	1
Field Scanline 2	40	21	1.9
Virtual Scanline 2	25	21	1.19
Field Scanline 3	49	25	1.96
Virtual Scanline 3	22	25	0.88

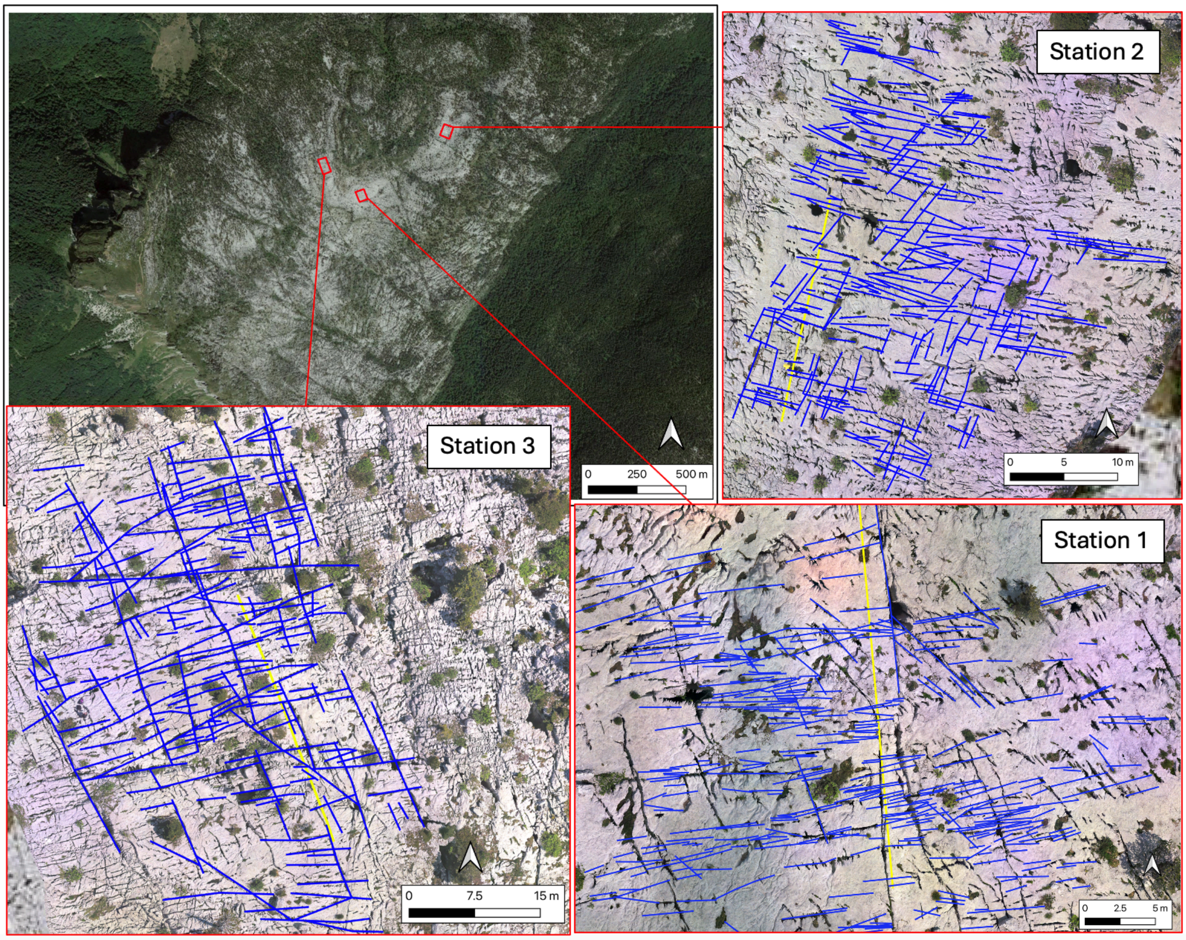

Figure 5.1: High-resolution drone image lineament interpretation (blue traces) including the field scanlines (yellow). Screenshots were taken at different zooms (see scale included in each map).

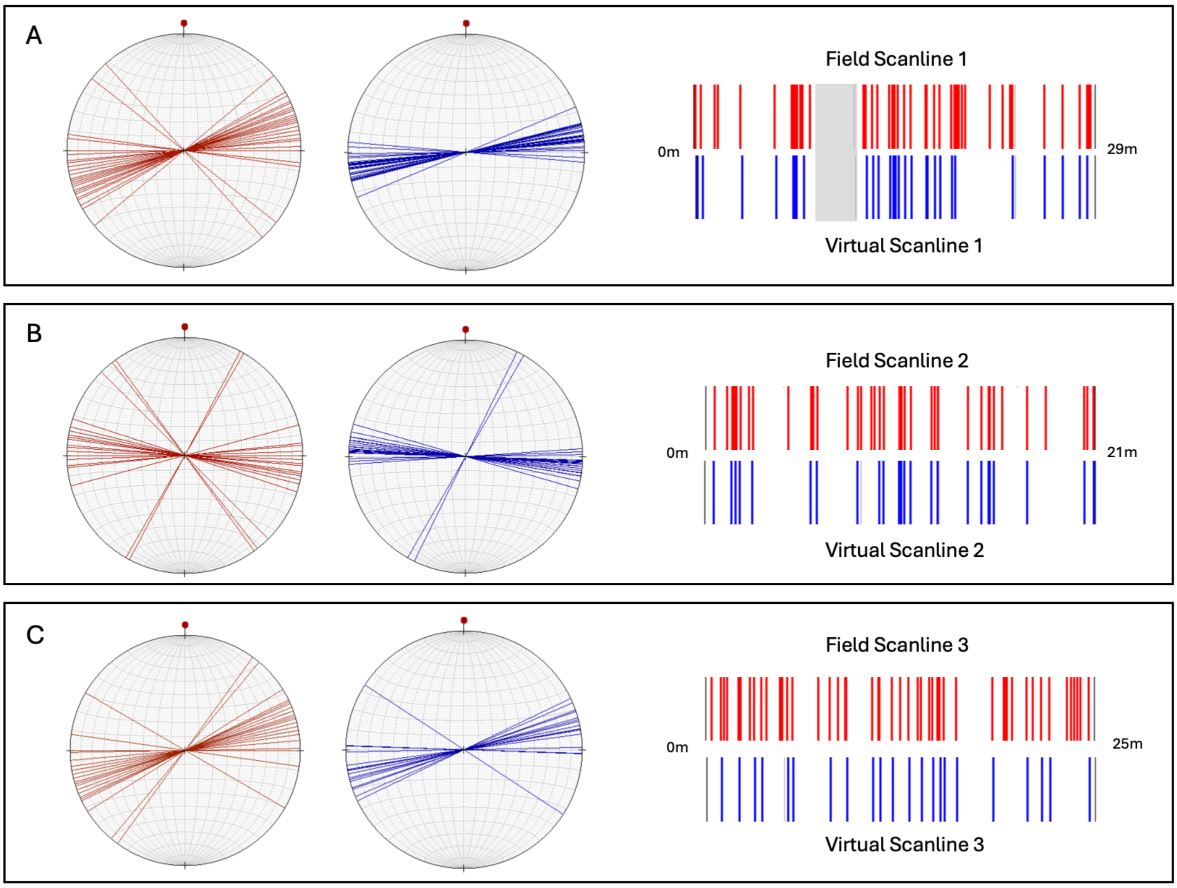

Figure 5.2: Field and virtual scanline comparison. Red stereonets and barcodes show the field scanline data, and blue is the virtual scanline data. Stations 1 to 3 are represented from A to C. The grey gap in barcode A represents scanline crossing a karst feature where no data was recorded.

5.2.2. Fracture Sets and Assosiations

Fracture sets were defined for field scanlines and the traced lineament interpretations at each station. This was done based on fracture orientation, Fisher K value and the orientation mean, mode and median. Furthermore, field descriptions, type of discontinuity and cement colour, were accounted for when defining sets.

Fisher K value is a measure of the concentration or dispersion of angles in a circular dataset (such as a stereonet). The magnitude of Fisher's K value indicates the degree of concentration of data points around the mean direction. A higher K value signifies a greater concentration of data points around a mean, and a lower K value indicates a more dispersed distribution. Furthermore, if the mode and the median values are closer to the mean value, the dataset is centred around a particular point (no significant skew in the data).

Station 1 (figure 5.1) data shows two preferred orientations: EW and NW-SE (figure 5.3). Fisher K value is plotted for both orientations (figure 5.3), orientation distribution and the mean, mode and median are calculated. Dataset with EW orientation is normally distributed with Fisher K value of 0.97 and mean 82.45, mode 73.90 and median 82.73 (see table 5.3). The high Fisher K value indicates that the dispersion is low, and the direction of the data is consistent. Therefore, we define a single-set oriented EW set. The NW-SE dataset has a lower Fisher K value, skewed orientation distribution, and a larger difference between the mean, mode, and median values. The dataset could be split in two: NW-SE (with a mean orientation strike of around 130 degrees) and NNW-SSE (with a mean strike of roughly 165 degrees). Only 3 discontinuities define the NNW-SSE set, whereas EW has 237 and NWSE 25 discontinuities.

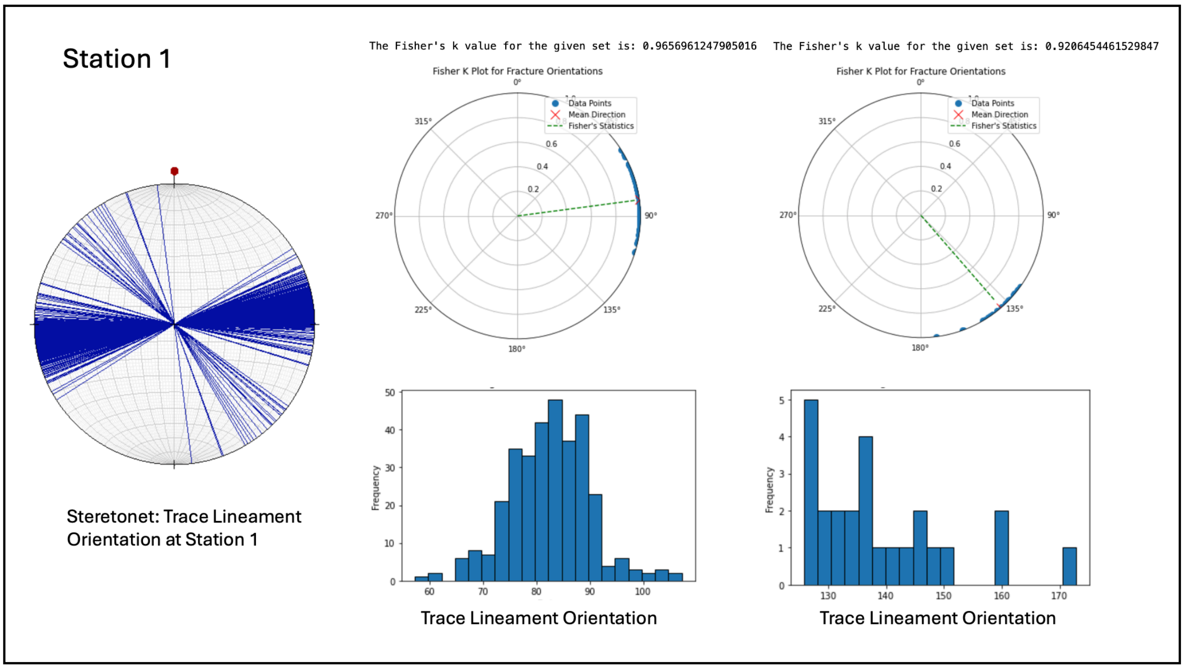

Figure 5.3: Example of Fisher K plots and orientation distributions for two datasets at Station 1.

Field scanline 1 also shows two preferred orientations: EW and NW-SE (figure 5.2 A). Fisher K was run for EW orientation, giving a value of 0.95, with mean 76.16, mode 78.0, and median 76.0. Analysis was not run for the NW-SE set due to the low number of discontinuities recorded (only 3).

Table 5.3: Fisher K results for three field scanlines and traced lineaments at three stations, as well as the mean, mode and median for each dataset.

	General Orientation	Number of Lineaments	Fisher K	Mean	Mode	Median
Scanline 1	EW	43	0.95	76.16	78.00	76.00
	NW-SE	3	-	-	-	-
Scanline 2	EW	30	0.96	94.87	98.00	94.00
	NW-SE	5	-	-	-	-
	NE-SW	5	-	-	-	-
Scanline 3	EW	46	0.95	72.06	70.00	71.00
	NW-SE	1	-	-	-	-
	NE-SW	2	-	-	-	-
Station 1	EW	327	0.97	82.45	73.90	82.73
	NW-SE	25	0.92	139.03	127.55	135.93
Station 2	EW	227	0.96	102.84	98.06	102.83
	NE-SW	75	0.95	28.29	18.51	27.00
Station 3	EW	134	0.95	77.42	80.05	77.39
	NWSE	56	0.92	155.20	116.02	157.85

Based on the orientation analysis, type of discontinuities and cement colour (if present), sets were defined for each station (table 5.5) and each field scanline (table 5.4). The following sets are recognized:

- D1 represents discontinuities striking roughly in the EW direction. After studying traced images, we noticed that D1 includes veins and vein arrays (en echelon). Therefore, D1 is not a single set, but an association. These veins and arrays were formed under the same stress conditions (principal stress orientations). Additionally, the cement colour is the same - grey to dark grey.

EW striking veins are the most abundant set in the field, as well as on the scanlines and drone images.

- Set D2 is defined as NW-SE striking veins (and karstified discontinuities), with white to light grey cement. D2 veins are not visible on drone images (virtual scanlines). This is most likely due to its colour (similar to the bedding colour) and image resolution. D2 was traced on the images, but only as karst.
- Set D3 represents NE-SW veins with light grey cement. There are no records of karstification for this set.
- Set D4 represents stylolites striking NNE-SSW. This set is most likely related to D1, as it forms under the same stress orientations. Set D4 is therefore a part of D1 association.
- Finally, set D5 is striking NNW-SSE, traced as karstified discontinuities at Stations 1 and 3.

Table 5.4: Field scanline sets and descriptions.

Scanline	Sets	Number of Discontinuities	Orientation Range	Type	Cement
Scanline 1	D1	43	EW 50 - 98	veins and karst	grey - dark grey
	D2	3	NWSE 128 - 138	karst	-
Scanline 2	D1	30	EW 75 - 108	veins and karst	grey - dark grey
	D2	5	NWSE 135 - 144	veins	white and light grey
	D3	5	NE-SW 28 - 30	veins	light gray
Scanline 3	D1	46	EW 58 - 98	veins and karst	gray - dark gray
	D2	1	NW-SE 120	karst	-
	D3	2	NE-SW 36-40	veins	light gray

Table 5.5: Sets identified from traced lineaments on high-resolution drone images.

Station	Sets	Number of Discontinuities	Orientation Range	Type	Cement
Station 1	D1	327	EW 57 - 107	veins, arrays, karst	grey - dark grey
	D2	22	NW-SE 125 - 150	veins karst	light grey
	D5	3	NNW-SSE 160 - 173	karst	-
Station 2	D1	227	EW 81-126	veins, arrays, karst	gray - dark gray
	D3	43	NE-SW 25 - 49	veins	light grey
	D4	32	NNE-SSW 8 - 24	stylolites and karst	grey
Station 3	D1	134	EW 43-98	karst	-
	D2	5	NW-SE 116-135	karst	-
	D5	51	NNW-SSE 143-180	karst	-

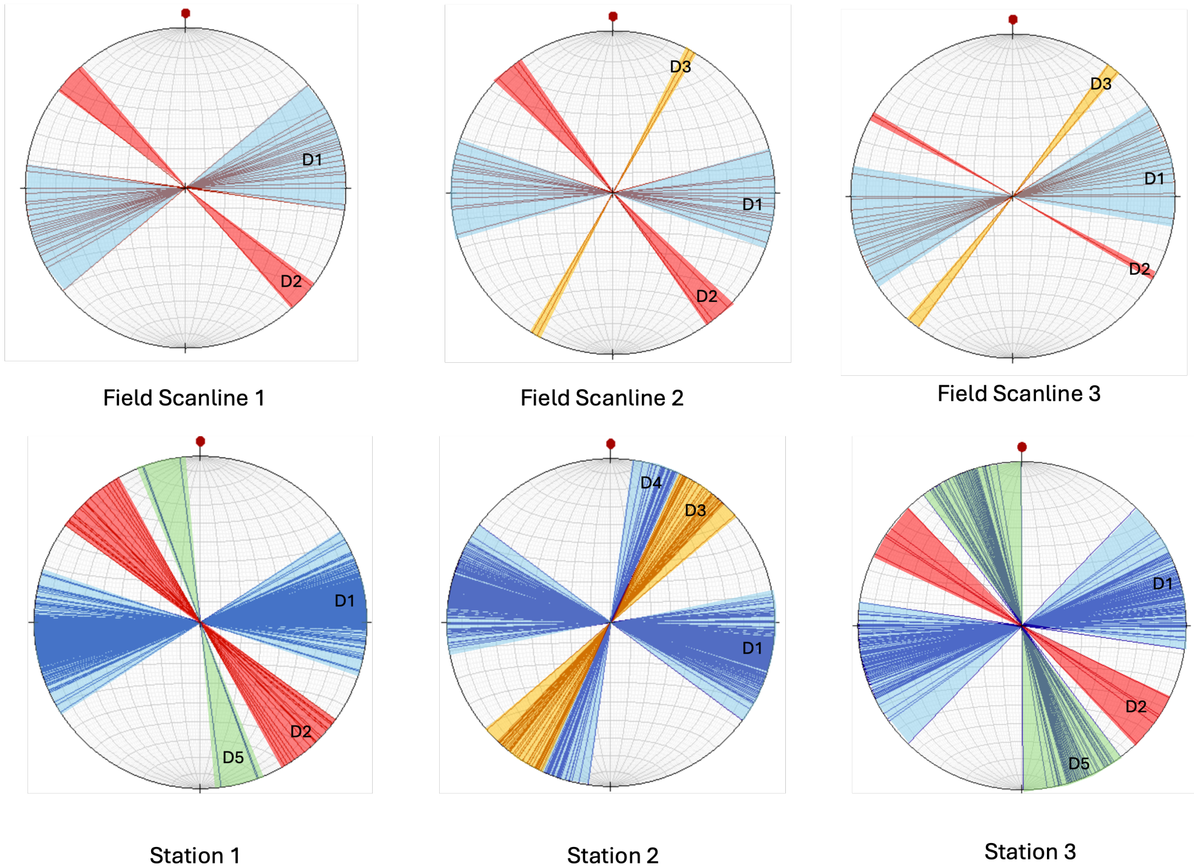

Figure 5.4: Sets identified on field scanlines (top), and sets on 1:10 traced pavements (bottom).

5.2.3. Length Analysis

Fracture length is a network property that is difficult to measure in the field.
Results show that discontinuities measured in the field as L are generally traced as M on the drone images. Many S and M discontinuities are not traced, and some M discontinuities are traced as S.

In general, fracture length is undersampled on drone images compared to the field observations. This can be due to image resolution, the presence of vegetation, the colour of discontinuities compared to the pavement, and/or the fracture aperture.

Additionally, S fractures are also less likely to be traced (figure 5.5). Virtual scanline 1 is missing 48% of S fractures, and these numbers increase to 58% and 77% on scanlines 2 and 3, respectively. Long fractures are least likely to 'be missed, however, they're usually traced as M. A similar applies to medium fracture, except on scanline 3 where 86% of the fractures were not traced.

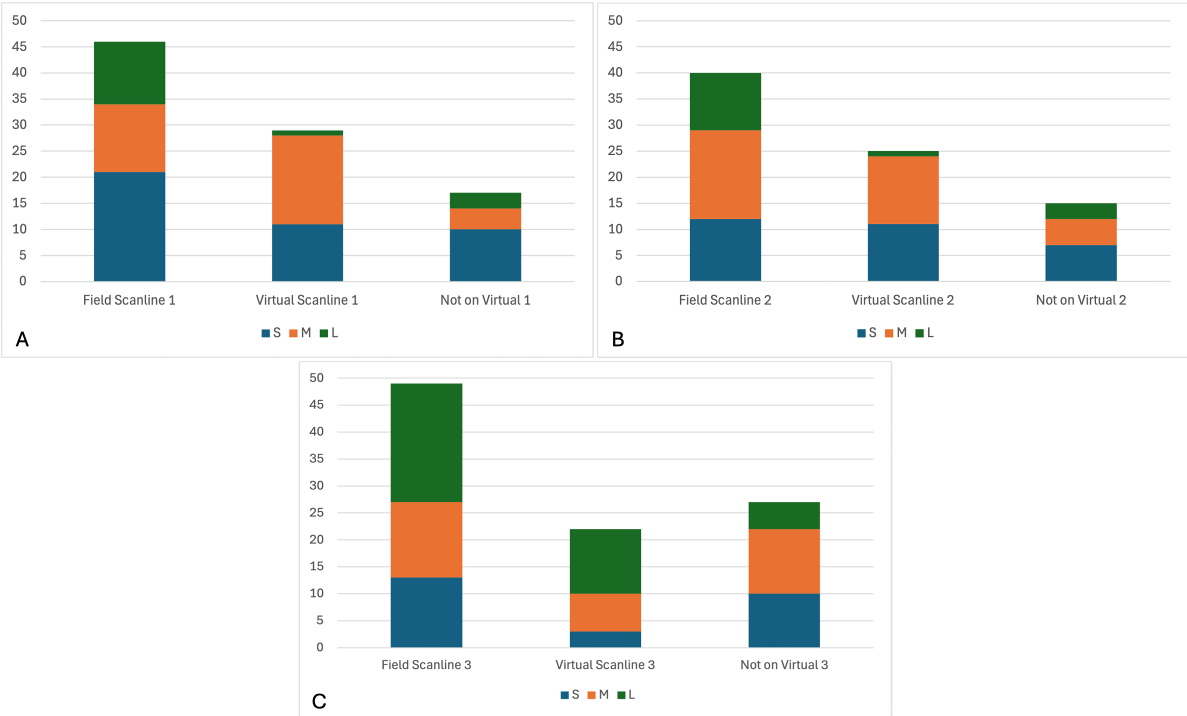

Figure 5.5: Lenght of fractures recorded on the field scanlines and traces on the virtual scanlines. 'Not on virtual' represents discontinuities recorded in the field but no traced on the drone images. A - station 1 results, B - station 2, and C - station 3 results.

5.2.4. Chapter Summary

One field scanline (30m) recorded by a student with some field experience took around an hour, whereas, one high-resolution flight covering an area of 70 by 75m (roughly $5.250m^2$) took only 14 minutes. However, manual fracture tracing is a time-consuming process. Tracing one image, with a traced area of around $1.200m^2$, took roughly 2 days (at 1:10 scale). On top of that, an additional day was needed to apply corrections.

After processing and comparing the field data with the drone data, we observe some differences in data quality. Field scanlines record all discontinuities intersecting the line, whereas we notice $35\% - 55\%$ of discontinuities missing from the manually traced lineaments. This is a significant amount, after analysing the data, we conclude that this is mainly due to the light grey cement colour present in some veins, which is similar to the pavement colour. Fracture visibility in the images depends on the resolution, pavement and cement colour, aperture, vegetation, and also on the weather. These resolution limitations cause truncation bias, which is evident when comparing scanlines and drone images. In the field, we preferred cloudy conditions as it reduced the number of shadows (from vegetation, or other objects). Furthermore, Virtual Scanline 3 only contains karstified discontinuities. Due to the high vegetation in the field, we couldn't fly the drone at $10m$ elevation, instead, we had to fly it at $15m$. This decreased the image resolution from $0.44cm/pix$ to $0.66cm/pix$. As we are interpreting veins on a cm-scale, this small reduction in the resolution made a significant difference, veins and non-karstified features were not visible.

When it comes to sets identified in the field and on the images, we notice the absence of set D2 on the Virtual Scanlines 1 and 2 (5.6). This is the set with light cement, not visible on UAV images. However, after interpreting the three Stations (the areas around scanlines), this set is traced at Station 1 and it appears at Station 3. We also notice sets D4 and D5 present at Station interpretations, but not on any scanlines. This is due to the limitations of collecting one scanline in the area. In order to get the full image of all the sets present at one station, multiple scanlines need to be taken at different orientations. Set D5 was missed on Scanline 3, as it was parallel to the Scanline itself. Set D4 did not intersect

Table 5.6: Fracture sets and their presence in field (scanlines), virtual scanlines and traced droned images (the three high-resolution stations).

	D1	D2	D3	D4	D5
Field Scanline 1	x	x			
Field Scanline 2	x	x	x		
Field Scanline 3	x	x	x		
Virtual Scanline 1	x				
Virtual Scanline 2	x		x		
Virtual Scanline 3	x				
Station 1	x	x			x
Station 2	x		x	x	
Station 3	x	x			x

Scanline 2, for the same reason. Scanlines were placed orthogonal to the EW set (set D1), the most abundant set in the field and on the UVA images. However, a minimum of two scanlines, of different orientations, are required in the field.

Besides the 'missing' fractures and sets, fracture length was also undersampled. Shorter discontinuities are less likely to be traced, and M and L are usually traced as S and M, respectively.

6

Fracture Network Multi-Scale Analysis

Fractures were digitised on UAV images at three scales: 1:500, 1:250 and 1:10. Additionally, satellite images were digitised at 1:7000 and 1:1000 scales. First, we compare the drone image trace maps. Three cases are considered based on location and area of interpretation (table 6.1). Case 1 covers Station 1 at 1:10 scale, and Stations 1 & 3 at 1:500 and 1:250 (same area, figure 6.1). Case 2 spatial cover increases as we decrease the scale (three different areas, figure 6.2). Finally, case 3 compares three scales within the same area of interpretation (same area at all scales, figure 6.3).

Table 6.1: We split and compare traced lineaments in 3 cases shown in this table.

	Location	Scale	Interpretation Area [m^2]	Number of Lineaments
Case 1	Station 1&3	1:500	51500	143
	Station 1&3	1:250	51500	341
	Station 1	1:10	1485	252
Case 2	Station 2	1:500	30450	44
	Station 2	1:250	12700	195
	Station 2	1:10	1400	302
Case 3	Station 3	1:500	2925	21
	Station 3	1:250	2925	47
	Station 3	1:10	2925	190

Mode I and II, stylolites and en echelon veins are only visible at 1:10 scale. At larger scales, only karstified fractures are visible and traced.

Manual digitisation of lineaments is a time-consuming process. Tracing at 1:10 scale took the most time, roughly 2 days of tracing (per station) and an additional 2 days to apply manual corrections. At higher scales tracing time is reduced, as fewer discontinuities are traced. A good example is case 3, where 190 lineaments were traced at 1:10 scale, and for the same area, 47 and 21 lineaments were traced at 1:250 and 1:500 scales, respectively. However, if we look at case 1 more lineaments were traced at 1:250 scale than at 1:10. This is due to the large increase in area. The interpretation of 1:250 area is almost 35 times larger than 1:10 area, and the increase in the number of lineaments is only 1.3 times. Interpretation time increases as we reduce the scale (zoom in).

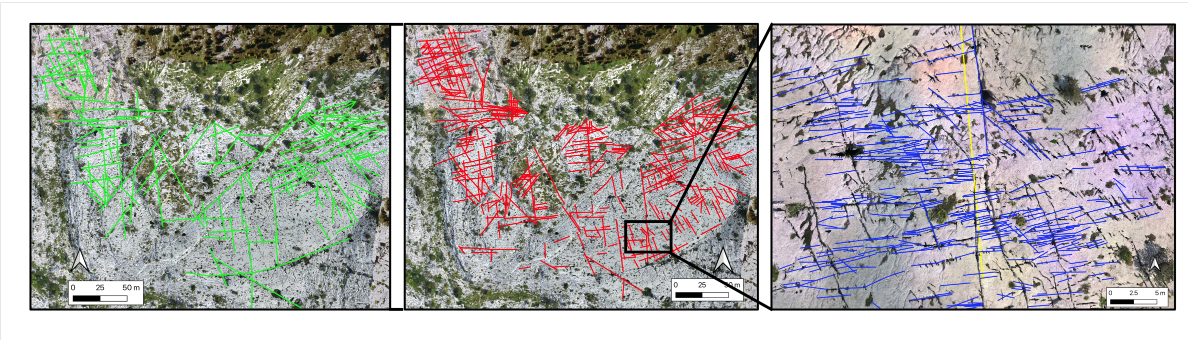

Figure 6.1: Case 1 - Scale from left to right: 1:500, 1:250 and 1:10.

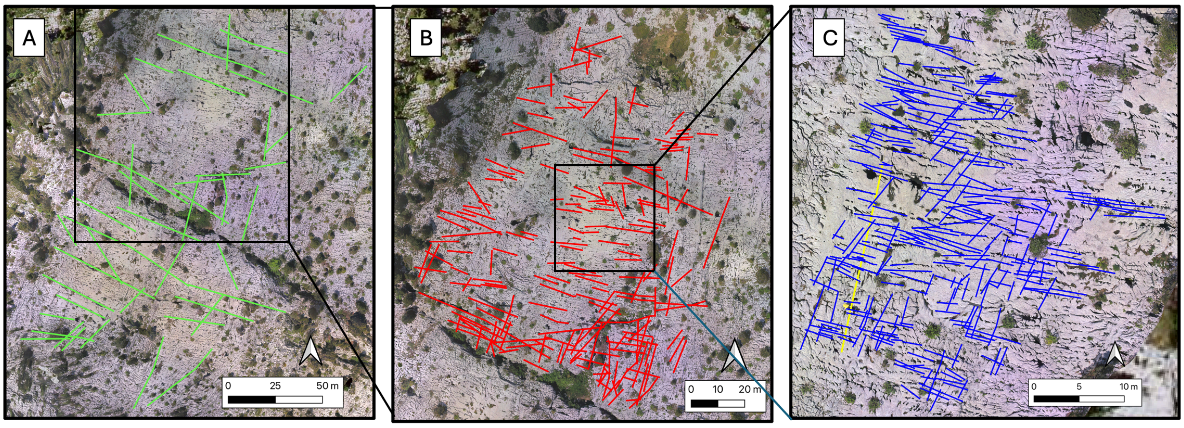

Figure 6.2: Case 2 - Scale from A to C: 1:500, 1:250 and 1:10.

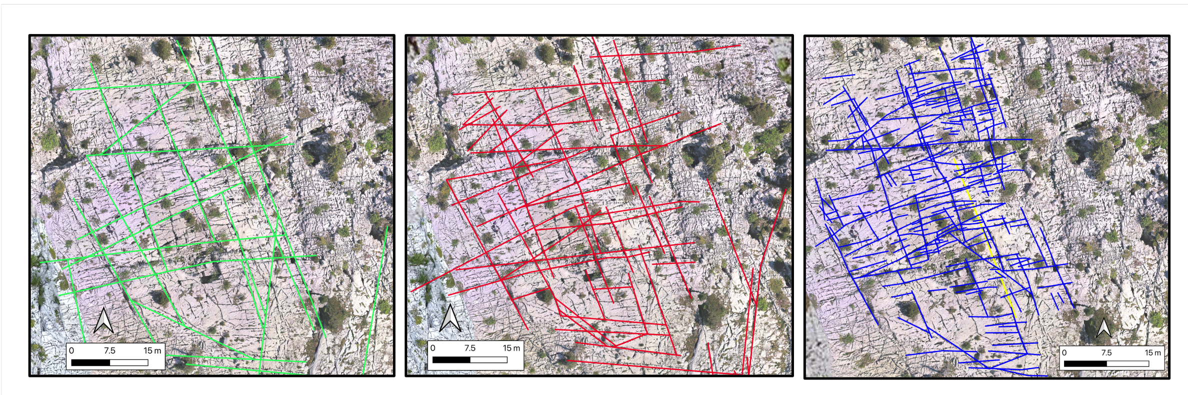

Figure 6.3: Case 3 - Scale from left to right: 1:500, 1:250 and 1:10. Lineaments traced at the same location and area at all three scales.

For each case variation in lineament orientation, length, density, intensity and topology at each scale has been studied and compared.

6.1. Variation of Fracture Orientation with scale

Rose diagrams consist of 36 bins (each 10 degrees), representing the frequency of traced lineaments.

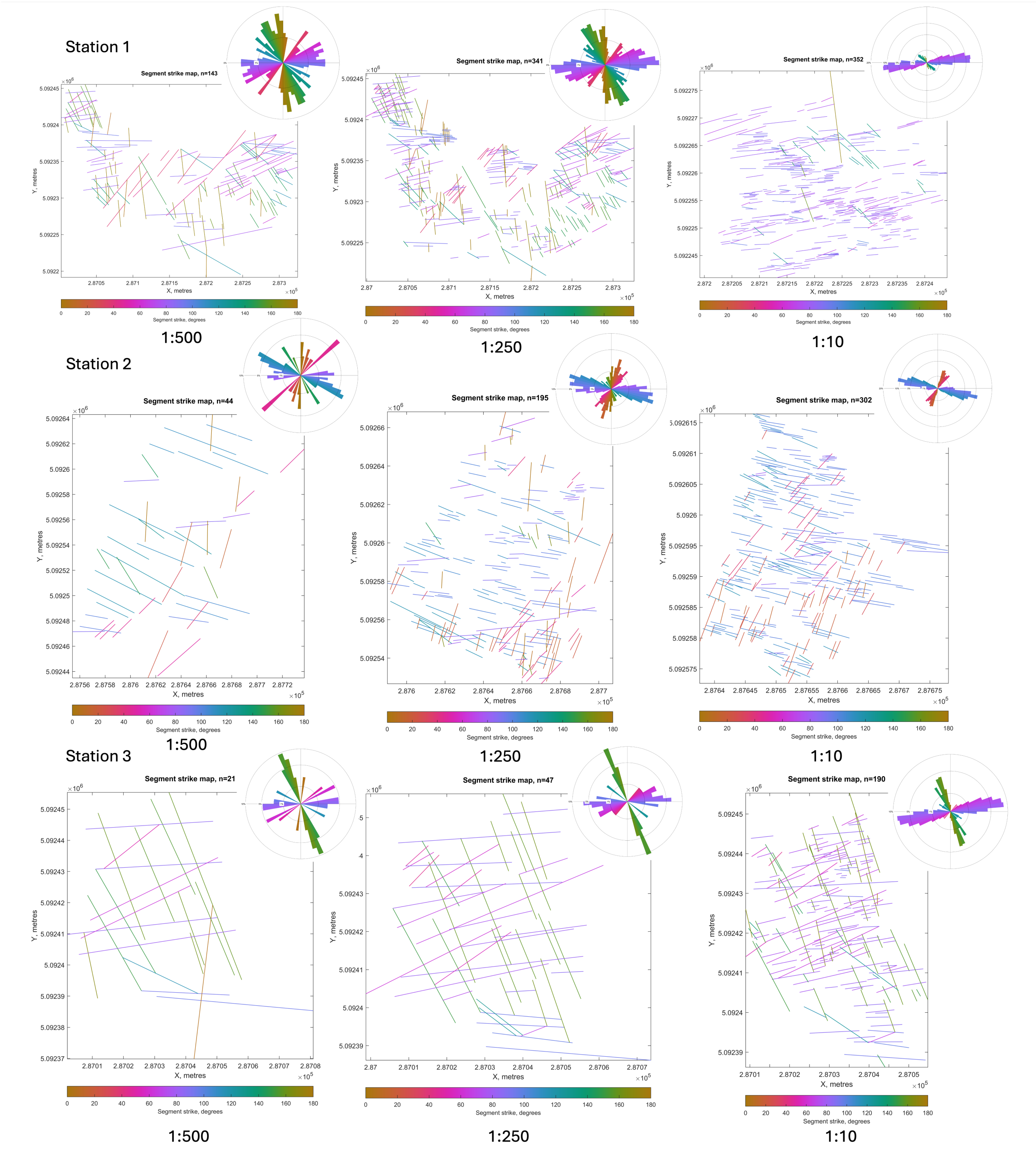

Figure 6.4: Lineament map with orientation frequencies for all 3 cases at all 3 scales.

At larger scales, lineament networks can be considered karst networks. Due to karstification and erosion, fracture mode cannot be determined, in the field or on the images. For this reason, these discontinuities cannot be grouped in sets based on fracture type. For example, at station 2, two sets have been identified with NESW orientation (chapter 5). These sets were defined based on fracture type: one being stylolites and the second mode I vein. However, this determination is not possible on scales 1:500 and 1:250. Sets can only be identified if trace maps are integrated with field survey data. Therefore, fractures have been grouped based on general orientation and sets identified in the field. Relative orientation abundance is shown in table 6.2. The orientation ranges were determined based on 1:10 interpretation shown in table 5.5, and based on orientation frequency.

Table 6.2: Relative orientation abundance at each scale.

	Relative abundance					
	Scale	EW	NW-SE	NE-SW	NNW-SSE	NS
Case 1	1:500	39%	9%	8%	27%	17%
	1:250	48%	9%	6%	25%	12%
	1:10	93%	6%	-	1%	-
Case 2	1:500	55%	9%	36%	-	-
	1:250	65%	6%	29%	-	-
	1:10	75%	-	25%	-	-
Case 3	1:500	45%	5%	-	50%	-
	1:250	60%	4%	-	36%	-
	1:10	70%	3%	-	27%	-

The most abundant orientation, across all scales and at each scenario is EW (exception: case 3 scale 1:500 - more variation due to very large area). With the increase of scale and area, the orientation range also increases. However, in most cases, the orientation trend is similar across different scales. Case 3 shows that the number of sets stays the same at each scale - therefore there is no orientation variability when the interpretation area stays the same. Most sets identified at 1:10 appear on higher scales, except NE-SW and NS-oriented traces in Case 1 (only present at 1:500 and 1:250), and NW-SE traces in Case 2 (present at 1:500 and 1:250). The variability is due to an increase in interpretation area as we increase the scale.

The strike of traced lineaments is shown to be scale-dependent. This is especially evident at satellite scales (1:1000 and 1:7000). At scale 1:10, three sets were identified (figure 5.4). As we move to 1:250 and 1:500, we notice that the orientation becomes more variable. This could be new sets, not traced on smaller scales. The EW (D1) set was the most abundant set in the field and at 1:10 scale, however, at 1:250 and 1:500 scales other sets dominate (figure 6.4). For example, in Cases 1 and 3 the most abundant set is the NW-SE, and in Case 2 it is the NE-SW set. Even though on a large scale (zoomed out) rose diagrams are more dispersed, three main orientations identified at 1:10 are still evident at 1:500 (figure 6.4). The variability of the network at a larger scale is most likely due to spatial heterogeneities and resolution. Therefore, we recommend 1:500 scale for lineament tracing of Parmelan anticline, integrated with field surveys.

6.2. Variation of Fracture Length with scale

Lineament length frequency is plotted on a binned graph and shows positively skewed distribution across almost all scales (exception in case 3 1:500 scale). Using FracPaQ's MLA analysis tool, the best-fitting power law, and exponential and lognormal scaling distributions for the trace length were calculated. Case 1 and Case 2 are best approximated by power law distribution, and exponential best fits Case 3 data (table 6.3). However, length trace data could be approximated using all three functions, as the difference is very subtle (6.3).

Table 6.3: Probability of trace lengths being power law, exponentially and log-normal distributed for each interpretation.

	Scale	Min Length [m]	Max Length [m]	Power Law [%]	Exponential [%]	Lognormal [%]
Case 1	1:500	16.56	153.66	99.12	98.6	98.16
	1:250	4.70	73.86	97.76	99.76	99.72
	1:10	0.65	16.83	99.68	99.04	96.36
Case 2	1:500	16.93	75.68	99.65	99.72	99.36
	1:250	3.20	54.35	99.36	98.48	99.28
	1:10	0.62	9.48	99.76	99.64	99.16
Case 3	1:500	21.60	64.50	99.46	99.56	99.52
	1:250	7.53	53.33	97.4	99.2	97.52
	1:10	1.40	36.44	92.68	96.56	95.4

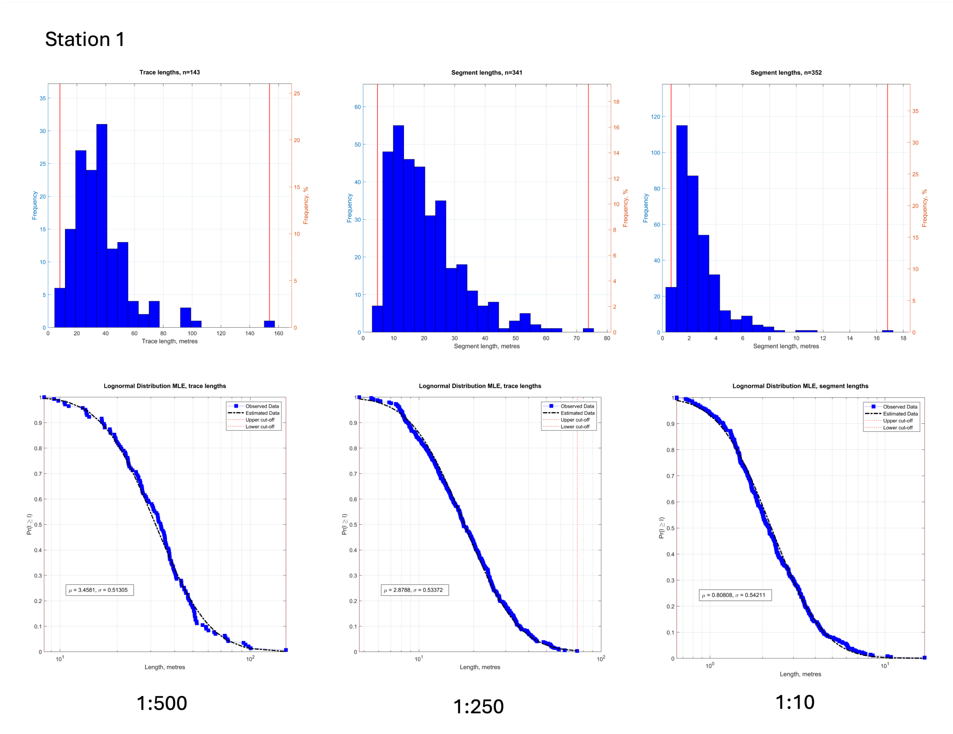

Figure 6.5: Histograms of lineament length in Case 1 at: 1:500, 1:250 and 1:10 scales. Red lines represent the minimum and maximum lengths. Below the histograms are lognormal distributions for trace lengths. Best fit line parameters are shown in text boxes on each plot (mean and standard deviation).

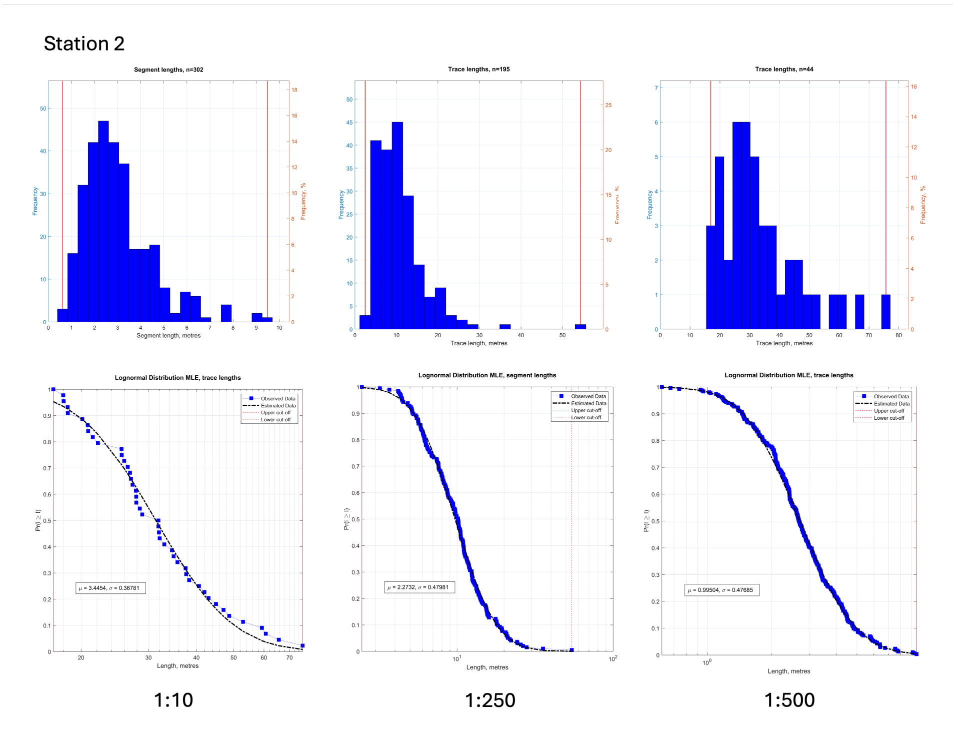

Figure 6.6: Histograms of lineament length in Case 2 at: 1:500, 1:250 and 1:10 scales. Red lines represent the minimum and maximum lengths. Below the histograms are lognormal distributions for trace lengths. Best fit line parameters are shown in text boxes on each plot.

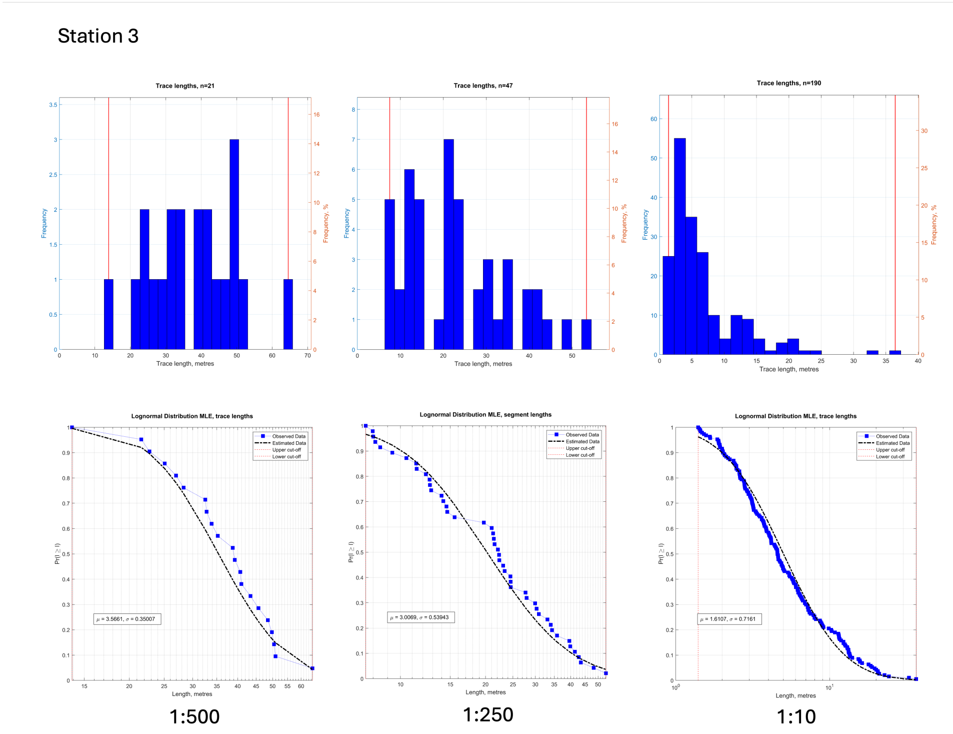

Figure 6.7: Histograms of lineament length in Case 3 at: 1:500, 1:250 and 1:10 scales. Red lines represent the minimum and maximum lengths. Below the histograms are lognormal distributions for trace lengths. Best fit line parameters are shown in text boxes on each plot.

Fracture length distribution histograms show consistent results with scale (figures 6.5, 6.6 and 6.7). Cases 1 and 2, where the interpretation area increases with the increase of scale, show positively skewed distributions. On the other hand, Case 3 shows that length distribution depends on scale and interpretation area. Here, we kept the area constant, and therefore, the length of longer discontinuities (at higher scales) was not captured due to the limited interpretation area. This is due to the censoring bias. Considering tracing time and length results, we would also recommend 1:500 for optimal analysis.

6.3. Variation of Fracture Density and Intensity with scale.

Density and intensity are shown to be scale-dependent properties. Both values increase with zoom increase. Even in Case 3, where the area is constant, higher P20 and P21 are related to higher zoom levels.

Table 6.4: Image interpretations are split in 3 cases. Note Case 3 has the same area for all three scales.

	Scale	Number of Lineaments	Length	Area	Intensity P21	Density P20
	1:500	143	5178.6	51500	0.100	0.003
Case 1	1:250	341	6989.4	51500	0.136	0.007
	1:10	252	924.4	1485	0.622	0.170
	1:500	44	1480.2	30450	0.049	0.001
Case 2	1:250	195	2134.3	12700	0.168	0.015
	1:10	302	914	1400	0.652	0.216
	1:500	21	785.9	2925	0.269	0.007
Case 3	1:250	47	1090.8	2925	0.373	0.016
	1:10	190	1252.7	2925	0.428	0.065

Fracture density (P20) represents the number of fractures per unit sampling area, and the intensity

(P21) is the length of fracture traces per unit sampling area. As expected, these values increase with zoom. The results show more similar P20 and P21 at 1:10 for Cases 1 and 2. This is due to the image resolution of Case 3 at 1:10. With higher image resolutions more fractures are visible and traced.

6.4. Variation of Topology with scale

Topology was analysed based on the proportions of isolated (I), abutting (Y), and crossing (X) nodes and summarized using ternary plots (figure 6.8, 6.9 and 6.10). For Case 1 we see that the proportion of nodes is very similar at 1:500 and 1:250 scale. At the smallest scale, the EW segments are largely dominant. This is because they are all parallel to each other the isolated nodes become dominant. The percentage of I nodes increases from 55% to 90%.

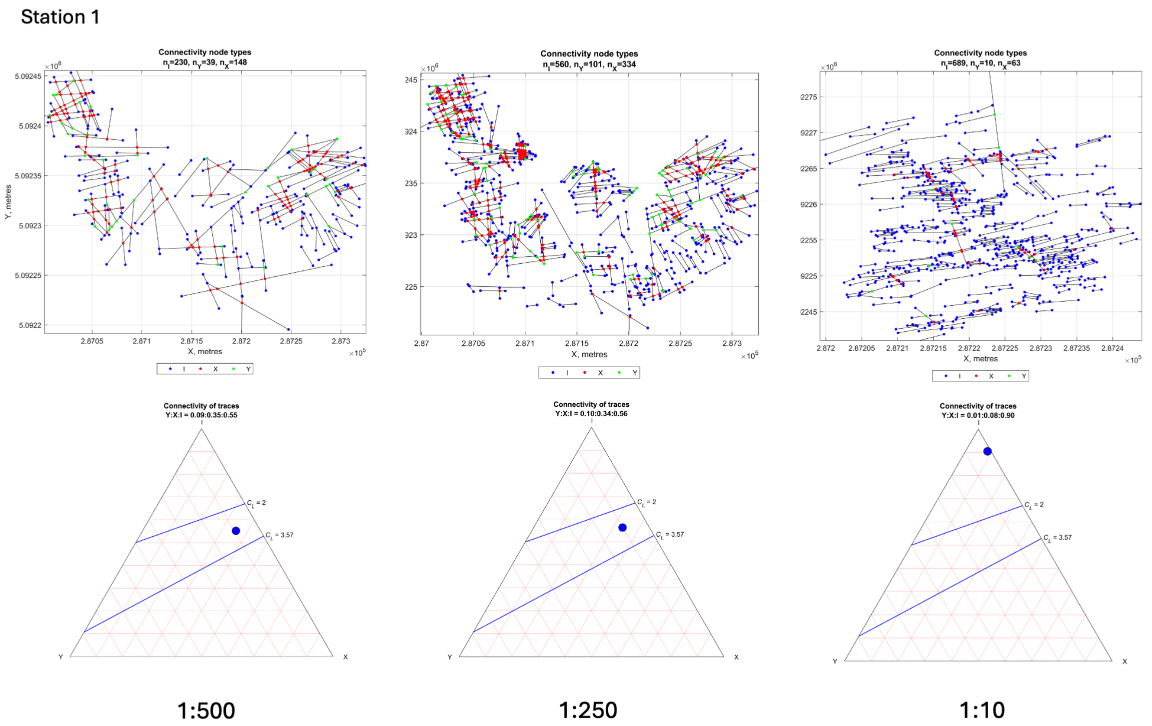

Figure 6.8: Ternary graphs for Case 1 across scales.

Case 2 shows high similarity in topology across all scales (figure 6.9). The percentage of Y, X and I nodes don't vary much across scales. Case 3 also shows similarities across higher scales, and at 1:10 scale we see an increase of I nodes at the expense of X nodes.

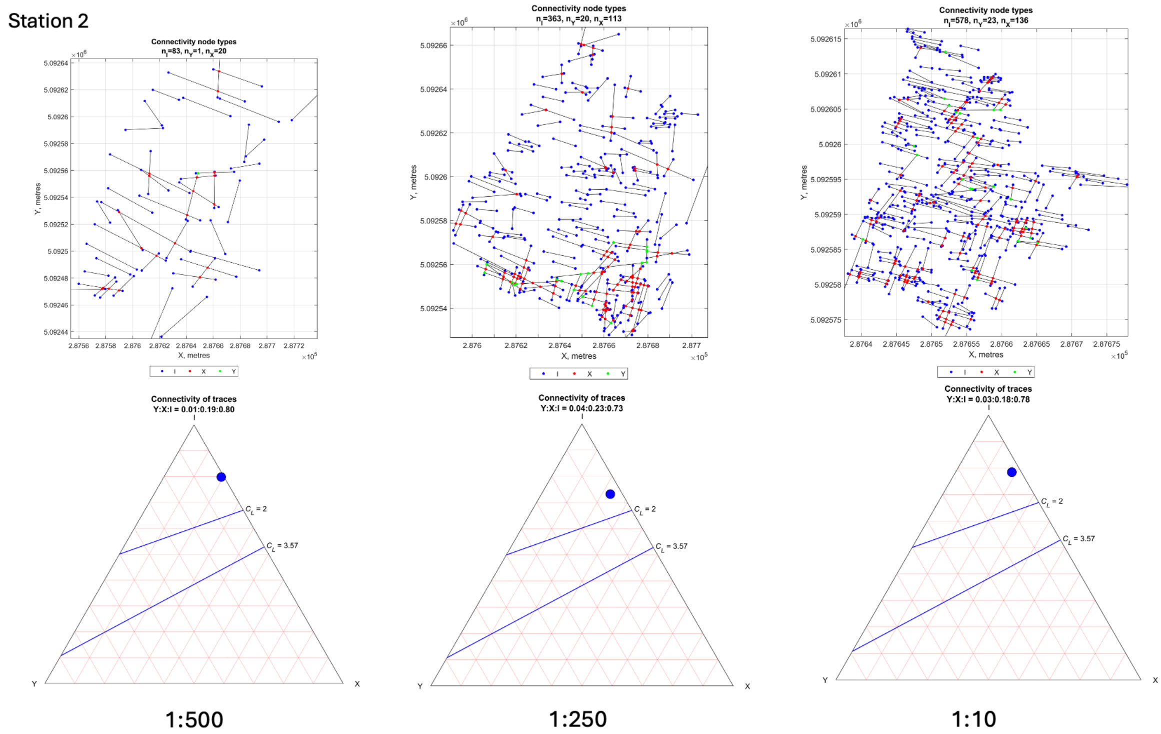

Figure 6.9: Ternary graphs for Case 2 across scales.

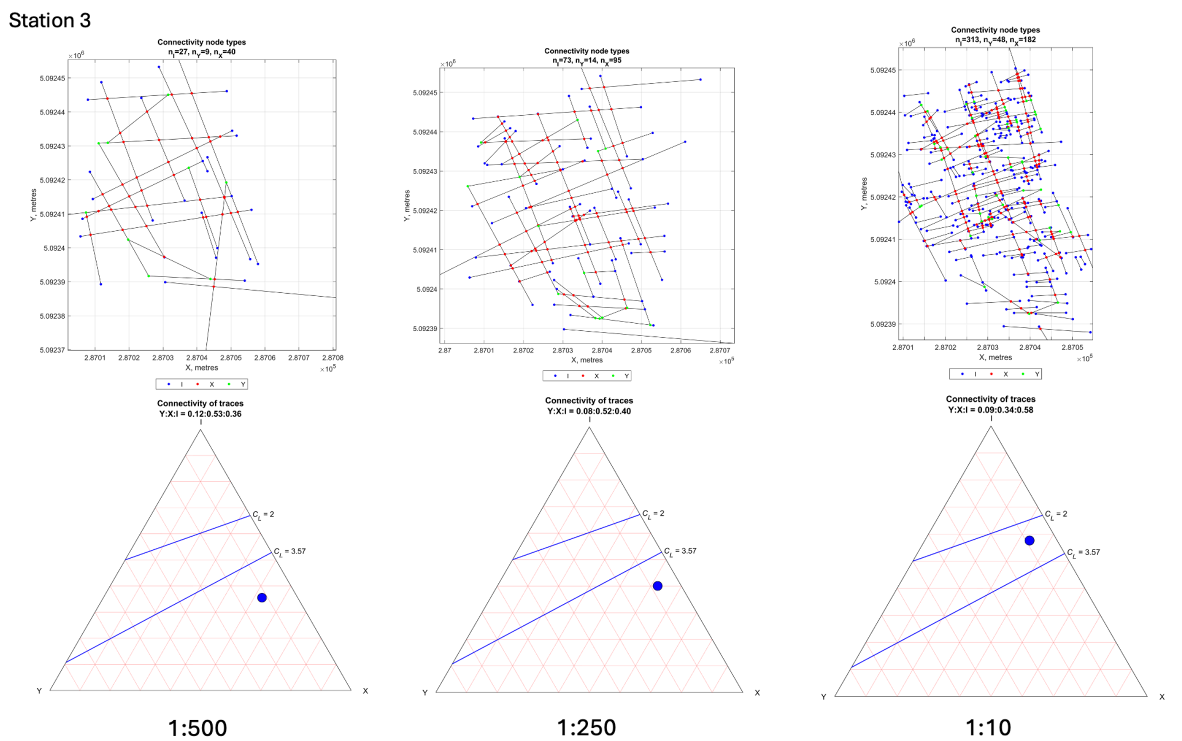

Figure 6.10: Ternary graphs for Case 3 across scales.

Topology is the only scale-independent property, focusing on the type of intersections between traced lineaments. This is why using the snapping tool in QGIS is important, otherwise many Y nodes would have been undersampled. Tertiary plots are essential in presenting topological data. These plots exhibit some similar results at different scales. The ratio of I, Y and X nodes is similar across different scales. It is interesting to see that, for example in Case 2, 1:10 interpretation plots similarly to 1:250 and 1:500. Case 1 shows a significantly larger number of I nodes at 1:10 compared to other scales. Here we notice a network consisting mostly of EW-oriented veins (93%)—lack of variation in orientation results in a network containing mostly I nodes.

Table 6.5: Table showing the number of I, Y and X nodes across different scales.

	Case 1			Case 2			Case 3		
Scale	1:500	1:250	1:10	1:500	1:250	1:10	1:500	1:250	1:10
I nodes	230	560	689	83	363	578	27	73	313
Y nodes	39	101	10	1	20	23	9	14	48
X nodes	148	334	63	20	113	136	40	95	182
No. nodes	417	995	762	104	496	737	76	182	543

6.5. Satellite Scale Results

Satellite images provide a 'full' picture of the anticline. They cover inaccessible areas, where drone imagery was not possible. Large-scale discontinuities (figure 6.11) are visible at this scale, which is important for understanding the geometry of the fold. These discontinuities are traced at 1:7000 and 1:1000, and it is evident, from the rose diagrams, that these networks are not comparable to smaller-scale structures.

Interpretation at scale 1:7000 (figure 6.11) shows the large-scale discontinuities traced in red (or faults according to Berio et al. 2021), or possibly fracture corridors (assumptions from our field observations). Two clear sets are visible, oriented NW and WNW. On the other hand, as we zoom in to 1:1000, the orientation of karst features is very variable. This interpretation follows the same rules set for smaller scales, however the results are very dispersed. Adapting new tracing rules for this scale could possibly improve the results.

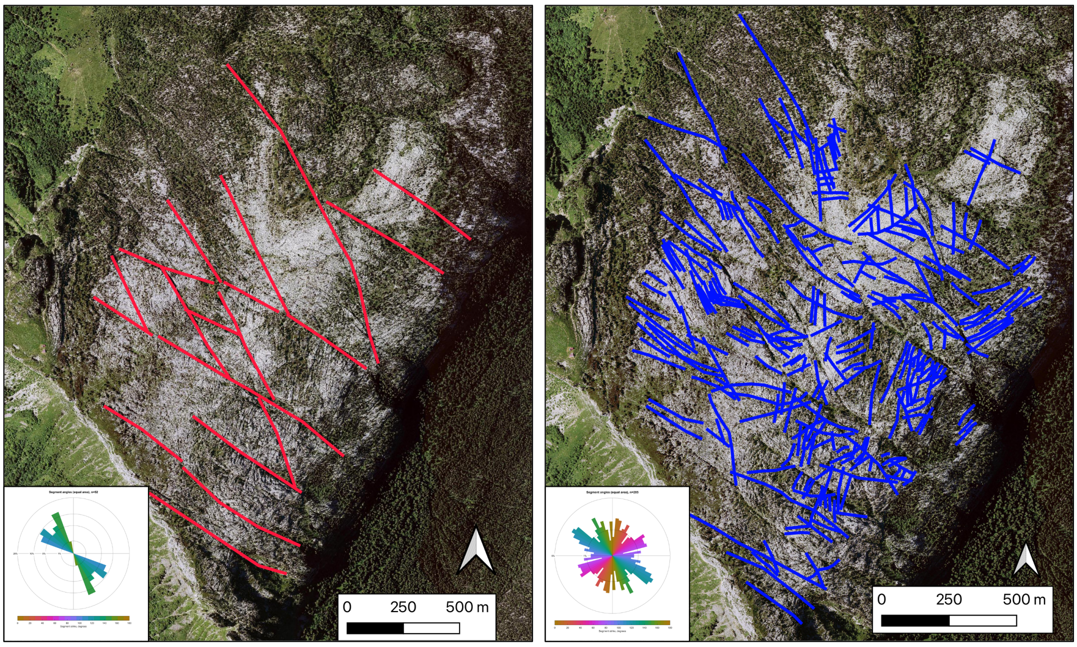

Figure 6.11: Trace maps at 1:7000 and 1:1000 scales, respectively.

7 Discussion

Results are analyzed, and their implications are discussed in relation to the following research questions:

- How can UAV imagery enhance the use of outcrop analogue data and complement traditional fieldwork?
- Do natural fracture networks show consistent patterns across different scales, allowing for predictive modelling of their geometry?

Furthermore, the limitations of the study are acknowledged, and recommendations for future research are proposed.

7.1. Advantages and Limitations of UAV data

In the past decade the use of UAV methods in geoscience has increased and the literature shows the following advantages:

- cost - this method is cheaper than other airborne methods (such as lidar) (Cawood et al. 2017).
- work time - according to Tibaldi et al. 2021 studying long structures (such as faults), is more optimal than field data collection.
- UAV allows studying inaccessible sites, vertical cliffs, or dangerous sites (i.e. active volcanoes) (Tibaldi et al. 2021).
- cm-scale resolution, allowing detail analysis (Tibaldi et al. 2021)

After comparing field scanline data to fractures traced on UAV images, the following has been observed: there is a difference in sets identified in field and UAV, and interpreting UAV images can be as time-consuming as fieldwork.

Three sets were recorded on field scanlines: EW (D1), NW-SE (D2) and NE-SW (D3). Virtual scanlines intersect only two sets: D1 and D3. Furthermore, $35\% - 55\%$ of total discontinuities recorded on field scanlines are 'missing' from the virtual scanlines. The absence of discontinuities from the drone images is most likely due to device resolution and cement colour. Even though, UAVs can achieve millimetre to centimetre scale resolution, the device was not able to capture all the data.

We further analysed the 1:10 lineament interpretation maps, and we identified two additional sets: NNE-SSE (D4) and NNW-SSE (D5). The absence of D4 and D5 from the scanlines is due to the limited number and coverage of scanlines, as well as the scanline orientations. Sets D4 and D5 have similar orientations as all three scanlines. As we increase the study area, from scanline to traced map, we notice that all sets are present, including D2. The small sample size (the scanlines) could explain the lack of D2 on virtual scanlines compared to the traced maps. However, this does not explain the absence of almost half of the discontinuities.

Although acquiring and processing drone images is a rapid process, interpreting UAV images at a 1:10 zoom level can be nearly as time-intensive as collecting scanline data directly in the field. UAV images produce greater outcrop coverage, however, more information regarding fracture characterisation can be collected in the field. This includes the type of discontinuity, dip angle, crossing relations, and aperture. This information is important when defining discontinuity sets and associations. In order to do this using drone (or satellite) images, field data must be integrated with traced lineament maps.

Even though using drones at the field (1:10) scale is shown not to be optimal, this method can be very useful for vertical clif and outcrops that are not accessible by foot. Furthermore, analysis at higher scales, as shown in this report, can optimize the fieldwork. Using UAVs is cheap and easy to manoeuvre.

Manual lineament tracing at 1:10 scale is not advised, after comparison with the traditional field collection method. Besides taking a lot of time, fracture characterisation is limited. Instead, a well-planned field campaign is recommended for studying fracture networks at this scale.

7.2. Multiscale Fracture Network Analysis

At 1:10 scale we trace fracture networks, and at higher scales (1:250, 1:500) we trace karst networks. We assume karst network formation is directly linked to fracture dissolution. This assumption is based on field observations and the consistency of stereonets across scales.

Two network parameters can be studied across multiple scales: variability and length. The variability of the network can be assessed using different parameters (orientation, density, intensity, connectivity...). For example, at 1:500 scale, we notice greater variability in lineament orientation, as well as orientation abundance (more dispersed data sets) compared to smaller-scale data. The variability is most likely due to rock heterogeneities. Lateral fracture network variability is present, the more we increase the sample area, the more variations in parameters are recorded.

Multi-scale analysis of fracture length shows that higher scales capture longer discontinuities, not measurable at field scale. Similar findings are shown by Mercuri et al. 2023, where fracture length is considered scale dependent property. Furthermore, we find that shorter fractures are less likely to be traced, which is also shown by Mauldon et al. 2001.

A concept of interpretation speed was introduced by Mercuri et al. 2023 (figure 7.1). This concept aligns with our study, where increasing the interpretation zoom will increase the interpretation time.

7.2.1. Fracture Network Similarity

Fractal networks refer to systems where the geometric properties, such as fracture lengths and spatial distribution, exhibit self-similar patterns over multiple scales. In geological formations, this implies that the patterns of fractures, regardless of the observation scale, follow a consistent distribution that can be described by fractal dimensions and power-law distributions (Odling 1997, Ovaskainen et al. 2023, Berkowitz et al. 2000). Theoretically, a slope of -2 often indicates scale invariance or self-similarity, which are key characteristics of fractals (Odling 1997). The slopes of the power law distribution of all the trace maps indicate values ranging from -13 to -4. These values don't indicate any statistical self-similarity of the network. These slopes signify a very steep decrease in the frequency of lineaments as their length increases. This is also evident from the frequency histograms (figure 6.5 for example).

To determine self-similarity in a distribution, you typically need to analyze the distribution's behaviour across multiple scales and observe if the same statistical patterns repeat at different levels of magnification. While certain slopes, such as -2, are more commonly associated with self-similar behaviour,

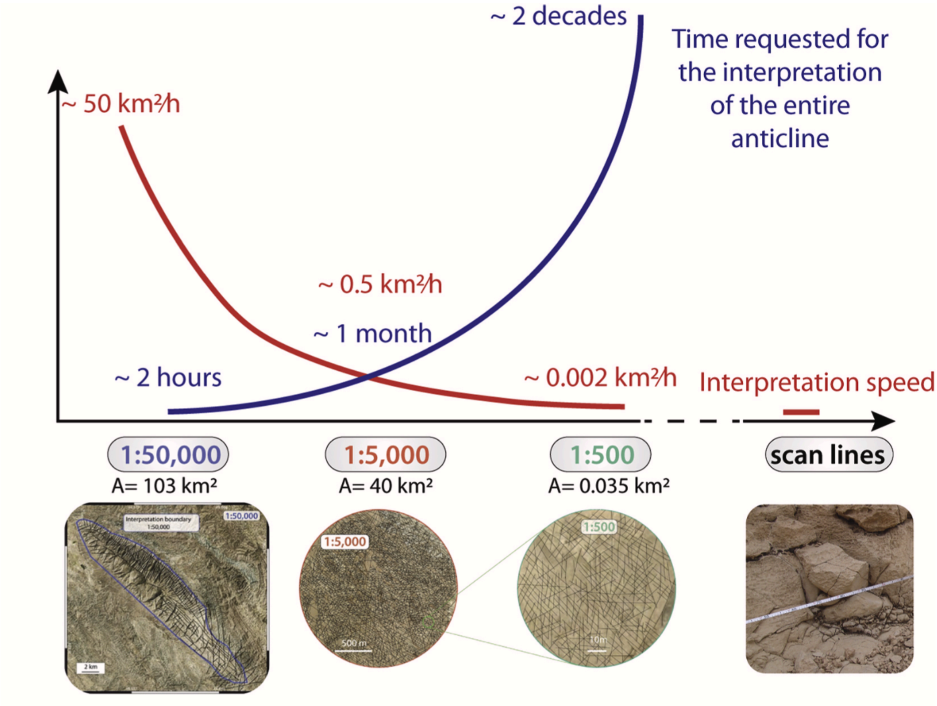

Figure 7.1: Fracture network analysis on different scales, from Mercuri et al. 2023.

a slope of -4 may still exhibit some degree of scale invariance depending on the specific context and characteristics of the data. Further analysis would be needed to confirm the presence of self-similarity. For example, Riley et al. 2011 uses correlation dimension and maximum Lyapunov exponent methods, where fracture dimension is determined by examining the differences between pairs of data points and by quantifying the irregularity or chaotic behaviour within a system, respectively. Furthermore, Sui et al. 2022 describes space syntax metric, the method evaluates spatial relationships and patterns within the network, focusing on how different parts of the network are interconnected.

If the fracture network is truly fractal, the patterns observed at one scale can be extrapolated to other scales. This means that if you know the fractal dimension, you can predict how the network will behave or appear at different scales. Fractal networks would allow us to, for example, project fracture network characteristics from satellite scale down to field scale, or from core data to outcrop scale. Fractals in natural fracture networks have been studied before, and many studies state that fracture networks behave like fractals (Watanabe and Takahashi 1995, Sui et al. 2022, Pavičić et al. 2023). However, multiple studies state otherwise (Odling 1992).

Besides fracture length, other network parameters can also show self-similar behaviour. For example, fracture orientation can exhibit fractal characteristics. This behaviour can be observed on rose diagrams. Trends in data across scales are evident, however further analysis is needed to determine if the behaviour is fractal. Fracture orientation, length and topology show similar results across scales.

7.2.2. Outcrop Analogue Data Optimisation

To complete an efficient fieldwork campaign, we suggest the following:

- Comparing field and drone data shows that censoring and truncation biases are common when focusing on a single data source. According to Bisdom et al. 2014 in order to prevent these biases outcrops should be interpreted from a range of observation scales in the field. For the Parmelan outcrop, integrating satellite (interpretation at 1:7000 scale), drone (at 1:500 scale) and field data would give a sufficient understanding of the network. Therefore, fieldwork should consist of taking drone images with a resolution of at least 2 cm/pix. For this study, this was achieved when flying the drone at 46m. At this altitude, there are no risks of high vegetation, and in 8 minutes drone covers an area of around 230m by 130m. At this resolution interpretation at 1:500 is possible.

- When collecting field data it is important to cover areas where variability would be expected. For example, data should be collected near the large-scale structures, and away from these structures. Furthermore, fracture variability can be expected at different parts of the fold structure. Therefore, measurements at the crest, and proximal to the limbs, should be taken.
- If scanlines are used as a field data method, at least two lines (of different orientations) should be taken at each location; or circular scanlines.

Fracture variability, specifically orientation variability can be captured relatively well using UAV images, as seen in table 5.6. Most of the sets are captured at Stations 1, 2 and 3, however, we know that many discontinuities are missing. Furthermore, when investigating fracture length we notice that many fractures cannot be traced fully. Discontinuities recorded in the field are longer than the same ones manually traced on the drone images. This is mainly due to image resolution, vegetation covering the pavement, aperture and colour contacts, and shadows. Orthomosaics are made of multiple overlapping images, and therefore, the full pavement orthomosaic can slightly vary in quality. If fracture lengths are not captured fully, as well as the number of fractures and orientations, then fracture density, intensity and topology are underrepresented. On the other hand, karstified discontinuities can be traced throughout their full length. The great aperture (from cm to m scale) and colour contrast are ideal for drone imagery. That being said, UAV is a great method to study karst networks, especially the length and variability, that can be difficult (and dangerous) in the field.

7.3. Fracture Network Associations

One of the aims of this report was to understand the behaviour of natural fracture networks, how it varies with scale and whether can it be simplified using geological rules. One of the methods of network simplification could be grouping individual fractures into sets, and further into fracture associations. Multiple associations can be present at the same location, which would indicate a switch in stress conditions.

In order to identify fracture associations, we need: fracture type and orientation. From this study we find that it is not possible to identify fracture type from UAV images alone, field work is necessary. Fracture orientations can be derived from the images, however, results are more reliable when integrated with field data. For example, if we assume that a certain orientation is always a stylolite, we can trace them into large-scale images. Therefore, the classification of fractures is essential. From this associations at large scales can be determined.

7.4. Fracture Network Implications for Geothermal Reservoirs

Fracture networks have significant implications for geothermal reservoirs, influencing their productivity, efficiency, and sustainability. Understanding the characteristics of these networks is crucial for successful geothermal energy extraction. One of the main implications of fracture network data is that it can be used to populate future DFN models and improve the understanding of the reservoir's behaviour.

If we assume that Parmelan is a representative analogue of a subsurface reservoir (in preparation: Hupkes 2024), the findings of this study can be used to make predictions about the reservoir. UAV and outcrop analogue data allow us to study fracture length and spatial variability, as shown in this report. These parameters cannot be determined from core or seismic data. This study can fill the gap between core and seismic data already available for the Canton of Geneva's geothermal project.

Fractures have been studied in wells, and the presence of the most abundant set in the field, the EW set, is also identified in well data (Doesburg 2023). Furthermore, Doesburg 2023 recognizes the NE-SW set as mode 2 fractures. Additionally, karst was also identified in the existing wells.

Understanding fracture types is important as they can have a different impact on reservoir permeability. For example, mode I fractures can act as fluid pathways, or in case of cementation (veins) they can prevent fluid flow. Stylolites can also act as conduits for flow, depending on their maturity (Bruna et al. 2019).

7.5. Recommendations

One of the main limitations of individual fracture interpretation is that it creates subjective bias. Peacock et al. 2019 compares fieldwork results of 40 students, and Doesburg 2023 compares well interpretation of 5 people. Both studies suggest additional steps in preventing, or reducing, these biases.

Based on all the multi-scale parameter results and lineament tracing times, scale 1:500 is shown to be the most optimal choice when integrated with fieldwork results. Studying networks below this scale could be possible in the future, with the improvement of automatic tracing. Automatic tracing was also attempted on a fractured sandstone outcrop from Nothern Territory, Australia. Even though there is no karstification, fractures are well visible on images, and there are no major erosion features (in the traced area), automatic tracing was not successful (figure 7.3).

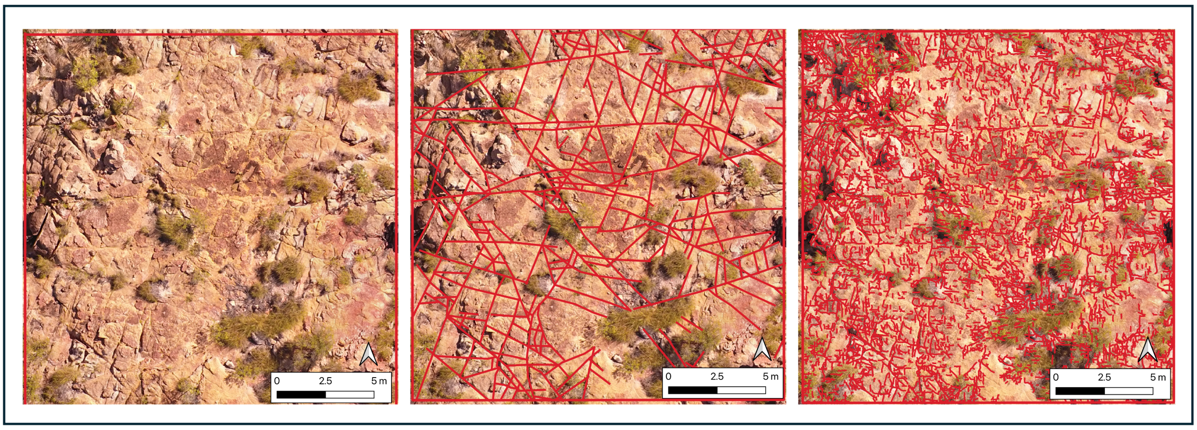

Figure 7.2: UAV image of Southern Lost City, Australia. Comparison of manual vs automatic tracing.

It could be interesting to further identify fracture associations, from field scale (1:10) to outcrop scale (1:500).

After tracing the network, further analysis is recommended using statistical methods. For example, using point process statistics described by Corrêa et al. 2022 to quantify spatial arrangement. Wang et al. 2019 uses the normalized correlation count method to discriminate clustered from randomly placed or evenly spaced patterns. Furthermore, Prabhakaran et al. 2021 combines different methods to analyse the spatial variation of a fracture network.

Berio et al. 2022 studies in detail veins cement in Parmelan. An interesting approach for further studies would be linking the cement to karst dissolution. Are specific sets more likely to dissolve and form karts? If so, this would have a great impact on how we model the fracture network.

	Cal-1 Cal-1 “type”	Cal-2	Cal-3	Cal-4	Cal-5
V1	X	X			D2
V4	X	X	X	X	D3
V5		X	X		D1

Figure 7.3: Example of cement types identified by Berio et al. 2022 and linked to fracture sets identified in the field.

8 Conclusion

This thesis demonstrates that integrating UAV imagery with traditional geological fieldwork provides a great tool for studying fracture networks of exposed outcrops. The high-resolution data obtained from UAVs allow for extensive and detailed mapping of fracture networks over large and otherwise inaccessible areas. However, the study also identifies significant limitations associated with UAV imagery, particularly in accurately identifying fracture types and therefore the associations. These limitations require incorporating traditional field data to complement and validate UAV findings.

The comparison between field data and UAV imagery reveals that approximately 35% to 55% of fractures identified in the field are not captured in UAV imagery. This discrepancy is primarily due to the limitations in image resolution, the colour similarity between fracture cement and the surrounding rock, and environmental factors such as vegetation and lighting conditions. The study finds that fracture length is often undersampled in UAV imagery, with shorter fractures being particularly underrepresented.

The multi-scale analysis conducted in this research confirms that natural fracture networks exhibit self-similar behaviour to some extent across different scales, supporting the application of predictive rules for network geometry. However, the analysis also reveals scale-dependent variations, emphasizing the importance of considering multiple scales in geological studies. These findings are important for optimizing outcrop analogue data for use in subsurface geothermal reservoir modelling, and therefore enhancing the predictive accuracy and efficiency of geothermal energy extraction.

The study recommends enhancing UAV techniques and incorporating more comprehensive field data to overcome existing limitations. Future research should focus on exploring advanced methods for automatically tracing fractures on aerial imagery, as well as exploring methods for bias reduction. By addressing these challenges, the integration of UAV and field data can be further optimized, leading to more accurate characterization of fracture networks and more efficient geothermal energy extraction practices. The outcomes of this research contribute to the development of more effective geological field methods and predictive models for geothermal reservoirs.

Bibliography

Bai, T. and Pollard, D. D. (2000). Fracture spacing in layered rocks: a new explanation based on the stress transition. *Journal of Structural Geology*, 22(1):43–57.

Berio, L. R., Balsamo, F., Mittempergher, S., Mozafar, M., Storti, F., Bistacchi, A., Bruna, P., and Bertotti, G. (2018). Deformation pattern in the thrust-related parmelan anticline (bornes massif, subalpine chains, haute-savoie, france): preliminary results. In *The EGU General Assembly*, page 8923.

Berio, L. R., Mittempergher, S., Storti, F., Bernasconi, S. M., Cipriani, A., Lugli, F., and Balsamo, F. (2022). Open–closed–open palaeofluid system conditions recorded in the tectonic vein networks of the parmelan anticline (bornes massif, france). *Journal of the Geological Society*, 179(5).

Berio, L. R., Storti, F., Balsamo, F., Mittempergher, S., Bistacchi, A., and Meda, M. (2021). Structural evolution of the parmelan anticline (bornes massif, france): Recording the role of structural inheritance and stress field changes on the finite deformation pattern. *Tectonics (Washington, D.C.)*, 40(11).

Berkowitz, B., Bour, O., Davy, P., and Odling, N. E. (2000). Scaling of fracture connectivity in geological formations. *Geophysical Research Letters*, 27(14):2061–2064.

Bertotti, G., Bisdom, K., Van Eijk, M., Hameka, F., Vis, A., Bezerra, H., and Reijmer, J. (2014). Fractures and fracture networks in carbonate reservoirs: A geological perspective (abstract). In *AAPG International Conference and Exhibition*, Istanbul, Turkey.

Bertotti, G., De Graaf, S., Bisdom, K., Oskam, B., Vonhof, H. B., Bezerra, F. H. R., Reijmer, J. J. G., and Cazarin, C. L. (2017). Fracturing and fluid□flow during post□rift subsidence in carbonates of the jandaíra formation, potiguar basin, ne brazil. *Basin Research*, 29(6):836–853.

Bisdom, K., Gauthier, B. D. M., Bertotti, G., and Hardebol, N. J. (2014). Calibrating discrete fracture-network models with a carbonate three-dimensional outcrop fracture network: Implications for naturally fractured reservoir modeling. *AAPG Bulletin*, 98(7):1351–1376.

Bisdom, K., Nick, H. M., and Bertotti, G. (2017). An integrated workflow for stress and flow modelling using outcrop-derived discrete fracture networks. *Computers & Geosciences*, 103:21–35.

Blatnik, M., Culver, D. C., Gabrovšek, F., Knez, M., Kogovšek, B., Kogovšek, J., Hong, L., Mayaud, C., Mihevc, A., Mulec, J., Năpăruş□Aljančič, M., Otoničar, B., Petrič, M., Pipan, T., Prelovšek, M., Ravbar, N., Shaw, T., Slabe, T., Šebela, S., and Hajna, N. Z. (2020). Lithomorphogenesis of karst surface. In *Advances in Karst Science*, pages 33–98. Springer.

Boersma, Q., Athmer, W., Etchebes, M., Haukås, J., and Bertotti, G. (2019). Natural fracture prediction: a multiscale integration of seismic data, image logs and numerical forward modelling. In *81st EAGE Conference and Exhibition 2019*.

Boersma, Q., Hardebol, N., Barnhoorn, A., and Bertotti, G. (2018). Mechanical factors controlling the development of orthogonal and nested fracture network geometries. *Rock Mechanics and Rock Engineering*, 51(11):3455–3469.

Bruna, P. O., Lavenu, A. P. C., Matonti, C., and Bertotti, G. (2019). Are stylolites fluid-flow efficient features? *Journal of Structural Geology*, 125:270–277.

Cawood, A. J., Bond, C. E., Howell, J. A., Butler, R. W., and Totake, Y. (2017). Lidar, uav or compass-clinometer? accuracy, coverage and the effects on structural models. *Journal of Structural Geology*, 98:67–82.

Clerc, N., Rusillon, E., Moscariello, A., Renard, P., Paolacci, S., and Meyer, M. (2015). Detailed structural and reservoir rock typing characterisation of the greater geneva basin, switzerland for geothermal resource assessment. In *World Geothermal Congress*, Melbourne, Australia.

Corrêa, R. S., Marrett, R., and Laubach, S. E. (2022). Analysis of spatial arrangement of fractures in two dimensions using point process statistics. *Journal of Structural Geology*, 163:104726.

Daniau, F., Aug, C., Lemaux, T., Lalou, R., and Lemaire, O. (2008). An innovative and multi-disciplinary methodology for modelling naturally fractured reservoirs. In *70th EAGE Conference and Exhibition Incorporating SPE EUROPEC 2008*.

De Joussineau, G., Barrett, K. R., Alessandroni, M., Maux, T. L., and Leckie, D. (2016). Organization, flow impact and modeling of natural fracture networks in a karstified carbonate bitumen reservoir: an example in the grosmont formation of the athabasca saleski leases, alberta, canada. *Bulletin of Canadian Petroleum Geology*, 64(2):291–308.

Doesburg, M. (2023). Uncertainty reduction in image log fracture interpretation, and its implications to the geological history of the geneva basin, switzerland. In *https://repository.tudelft.nl/*.

Fossen, H. (2010). *Structural Geology*. Cambridge University Press.

Gale, J. F. W., Lander, R. H., Reed, R. M., and Laubach, S. E. (2010). Modeling fracture porosity evolution in dolostone. *Journal of Structural Geology*, 32:1201–1211.

Hardebol, N., Maier, C., Nick, H. M., Geiger, S., Bertotti, G., and Boro, H. (2015). Multiscale fracture network characterization and impact on flow: A case study on the latemar carbonate platform. *Journal of Geophysical Research: Solid Earth*, 120(12):8197–8222.

Healy, D., Rizzo, R. E., Cornwell, D. G., Farrell, N. J., Watkins, H., Timms, N. E., Gomez-Rivas, E., and Smith, M. (2017). Fracpaq: A matlab™ toolbox for the quantification of fracture patterns. *Journal of Structural Geology*, 95:1–16.

Hupkes, J. (2024). *PhD Thesis - In Preparation*. PhD thesis, Delft University of Technology. In preparation.

Kopf, A. J. (2006). Mervyn s. paterson and teng-fong wong, experimental rock deformation – the brittle field, 2005. *Surveys in Geophysics*, 27(4):487–488.

Lecompte, M. (2019). The geothermie2020 program: Supporting the development of geothermal resources use in gevena canton. In *AAPG 3rd Hydrocarbon Geothermal Cross Over Technology Workshop*, volume 3.

Lei, Q., Wang, X., Min, K.-B., and Rutqvist, J. (2020). Interactive roles of geometrical distribution and geomechanical deformation of fracture networks in fluid flow through fractured geological media. *Journal of Rock Mechanics and Geotechnical Engineering*, 12(4):780–792.

Lismonde, B. (1983a). Le réseau de la diau. *Karstologia*, 1(1):9–18.

Lismonde, B. (1983b). Le réseau de la diau. *Karstologia*, 1(1):9–18.

Manzocchi, T. (2002). The connectivity of two-dimensional networks of spatially correlated fractures. *Water Resources Research*, 38(9).

Marrett, R., Gale, J., Gomez, L., and Laubach, S. E. (2018). Correlation analysis of fracture arrangement in space. *Journal of Structural Geology*, 108:16–33.

Martinelli, M., Bistacchi, A., Mittempergher, S., Bonneau, F., Balsamo, F., Caumon, G., and Meda, M. (2020). Damage zone characterization combining scan-line and scan-area analysis on a km-scale digital outcrop model: The qala fault (gozo). *Journal of Structural Geology*, 140:104144.

Mauldon, M., Dunne, W. M., and Rohrbaugh, M. (2001). Circular scanlines and circular windows: new tools for characterizing the geometry of fracture traces. *Journal of Structural Geology*, 23(2–3):247–258.

Meda, M., Martinelli, M., Bistacchi, A., Mittempergher, S., Berio, L., Balsamo, F., Succo, A., and Storti, F. (2019). 3d multi-scale characterization and modeling of three fractured carbonatic outcrop analogues: Pag croatia, parmelan france, gozo maltese islands. In *Abu Dhabi International Petroleum Exhibition & Conference*, Abu Dhabi, UAE.

Mercuri, M., Tavani, S., Aldega, L., Trippetta, F., Bigi, S., and Carminati, E. (2023). Are open-source aerial images useful for fracture network characterisation? insights from a multi-scale approach in the zagros mts. *Journal of Structural Geology*, 171:104866.

Moscariello, A. (2019). Exploring for geo-energy resources in the geneva basin (western switzerland): opportunities and challenges. *Swiss Bulletin für angewandte Geologie*, 24(2):105–124.

Odling, N. E. (1992). Network properties of a two-dimensional natural fracture pattern. *Pure and Applied Geophysics*, 138(1):95–114.

Odling, N. E. (1997). Scaling and connectivity of joint systems in sandstones from western norway. *Journal of Structural Geology*, 19(10):1257–1271.

Ong, P. Y. and Jamaludin, S. N. F. (2023). Fracture network analysis of karstified subis limestone build-up in niah, sarawak. *Applied Sciences*, 13(22):12110.

Ovaskainen, N., Skyttä, P., Nordbäck, N., and Engström, J. (2023). Detailed investigation of multi-scale fracture networks in glacially abraded crystalline bedrock at Åland islands, finland. *Solid Earth*, 14(6):603–624.

Pavičić, I., Duić, Ž., Vrbaški, A., and Dragičević, I. (2023). Fractal characterization of multiscale fracture network distribution in dolomites: outcrop analogue of subsurface reservoirs. *Fractal and Fractional*, 7(9):676.

Peacock, D., Nixon, C. W., Rotevatn, A., Sanderson, D. J., and Zuluaga, L. F. (2016). Glossary of fault and other fracture networks. *Journal of Structural Geology*, 92:12–29.

Peacock, D., Sanderson, D. J., and Rotevatn, A. (2018). Relationships between fractures. *Journal of Structural Geology*, 106:41–53.

Peacock, D. C., Sanderson, D. J., Bastesen, E., Rotevatn, A., and Storstein, T. H. (2019). Causes of bias and uncertainty in fracture network analysis. *Norwegian Journal of Geology*.

PGG (2011). Evaluation du potentiel géothermique du canton de genève – vol. 1: Rapport final. Technical report, Service cantonal de l'énergie - Services Industriels de Genève.

Prabhakaran, R., Bertotti, G., Urai, J. L., and Smeulders, D. (2021). Investigating spatial heterogeneity within fracture networks using hierarchical clustering and graph distance metrics. *Solid Earth*, 12(10):2159–2209.

Prabhakaran, R., Bruna, P. O., Bertotti, G., and Smeulders, D. (2019). An automated fracture trace detection technique using the complex shearlet transform. *Solid Earth*, 10(6):2137–2166.

Ramsey, J. and Chester, F. (2004). Hybrid fracture and the transition from extension fracture to shear fracture. *Nature*, 428:63–66.

Ray, D. S., Al-Shammeli, A., Verma, N. K., Matar, S., De Groen, V., De Joussineau, G., Ghilardini, L., Maux, T. L., and Al-Khamees, W. (2012). Characterizing and modeling natural fracture networks in a tight carbonate reservoir in the middle east: A methodology. *Buletin Persatuan Geologi Malaysia*, 58:29–35.

Riley, P., Tikoff, B., and Murray, A. (2011). Quantification of fracture networks in non-layered, massive rock using synthetic and natural data sets. *Tectonophysics*, 505(1–4):44–56.

Rusillon, E. (2017). *Characterisation and rock typing of deep geothermal reservoirs in the Greater Geneva Basin (Switzerland & France)*. PhD thesis, University of Geneva.

Sanderson, D., Peacock, D., and Nixon, C. (2024). Fracture sets and sequencing. *Earth-Science Reviews*.

Sanderson, D. J. and Nixon, C. W. (2015). The use of topology in fracture network characterization. *Journal of Structural Geology*, 72:55–66.

Sanderson, D. J., Peacock, D., Nixon, C. W., and Rotevatn, A. (2019). Graph theory and the analysis of fracture networks. *Journal of Structural Geology*, 125:155–165.

Steijn, J. (2018). Fracture networl characterisation in the mcarthur basin, northern territory, australia,. Bsc thesis, Applied Earth Sciences, [Name of the University].

Sui, L., Wang, H., Wu, J., Zhang, J., Yu, J., Ma, X., and Sun, Q. (2022). Fractal description of rock fracture networks based on the space syntax metric. *Fractal and Fractional*, 6(7):353.

Sweeney, M., Hyman, J. D., O'Malley, D., Santos, J. E., Carey, J. W., Stauffer, P. H., and Viswanathan, H. (2023). Characterizing the impacts of multi-scale heterogeneity on solute transport in fracture networks. *Geophysical Research Letters*, 50(21).

Tibaldi, A., Corti, N., Beni, E. D., Bonali, F. L., Falsaperla, S., Langer, H., Neri, M., Cantarero, M., Reitano, D., and Fallati, L. (2021). Mapping and evaluating kinematics and the stress and strain field at active faults and fissures: a comparison between field and drone data at the ne rift, mt etna (italy). *Solid Earth*, 12(4):801–816.

Tóth, E., Hrabovszki, E., Tóth, T. M., and Schubert, F. (2020). Shear strain and volume change associated with sigmoidal vein arrays in the boda claystone. *Journal of Structural Geology*, 138:104105.

Veress, M. (2009). *Rinnenkarren*, volume 9, pages 211–222.

Wang, Q., Laubach, S. E., Gale, J. F. W., and Ramos, M. J. (2019). Quantified fracture (joint) clustering in archean basement, wyoming: application of the normalized correlation count method. *Petroleum Geoscience*, 25(4):415–428.

Wang, X., Aliouache, M., Wang, Y., Lei, Q., and Jourde, H. (2021). The role of aperture heterogeneity in incipient karst evolution in natural fracture networks: Insights from numerical simulations. *Advances in Water Resources*, 156:104036.

Watanabe, K. and Takahashi, H. (1995). Fractal geometry characterization of geothermal reservoir fracture networks. *Journal of Geophysical Research*, 100(B1):521–528.

Watkins, H., Bond, C. E., Healy, D., and Butler, R. W. (2015). Appraisal of fracture sampling methods and a new workflow to characterise heterogeneous fracture networks at outcrop. *Journal of Structural Geology*, 72:67–82.

Zeeb, C., Gómez-Rivas, E., Bons, P. D., and Blum, P. (2013). Evaluation of sampling methods for fracture network characterization using outcrops. *AAPG Bulletin*, 97(9):1545–1566.

A
Fracture Network Trace Maps

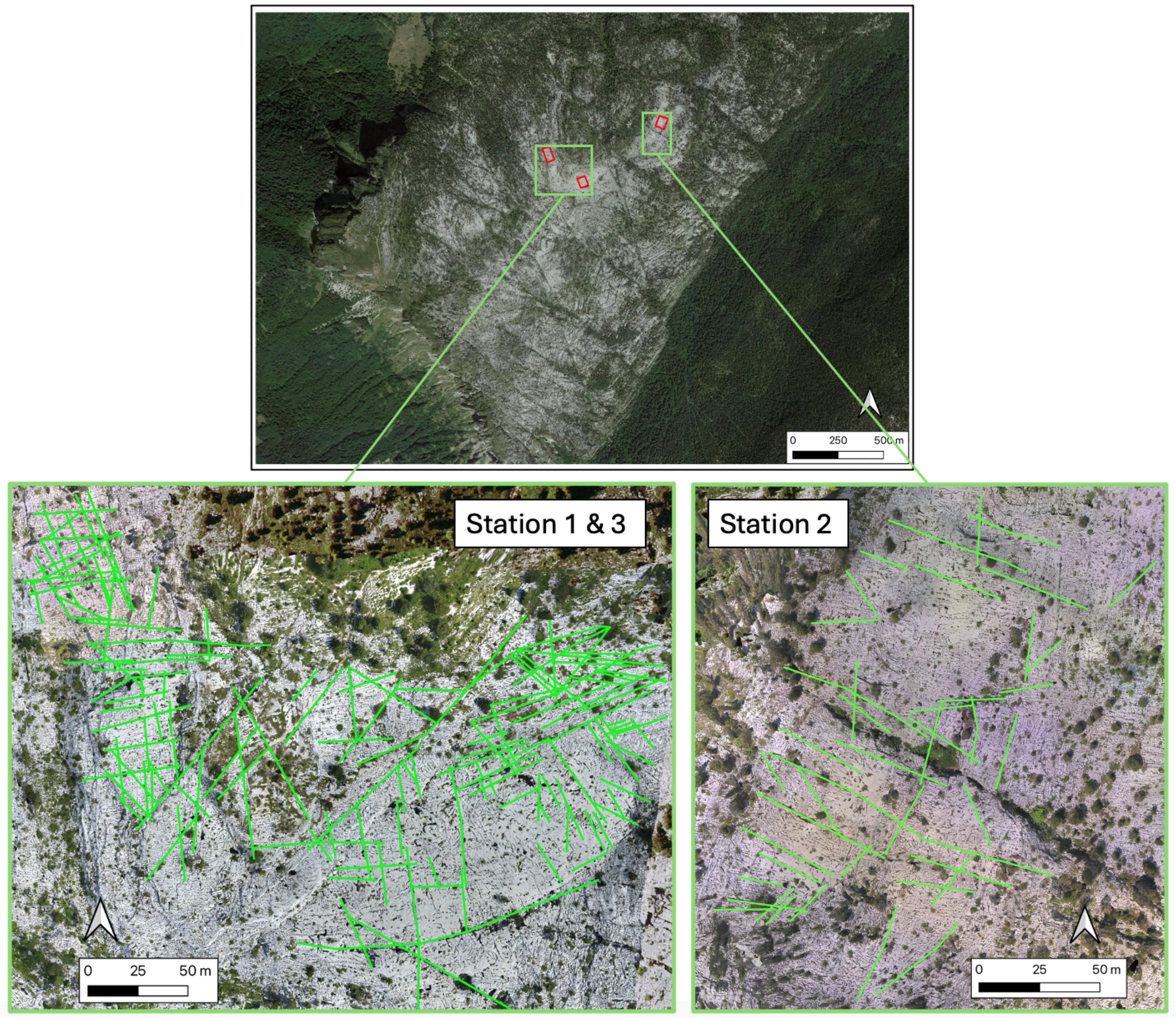

Figure A.1: Traced lineaments at 1:500 scale.

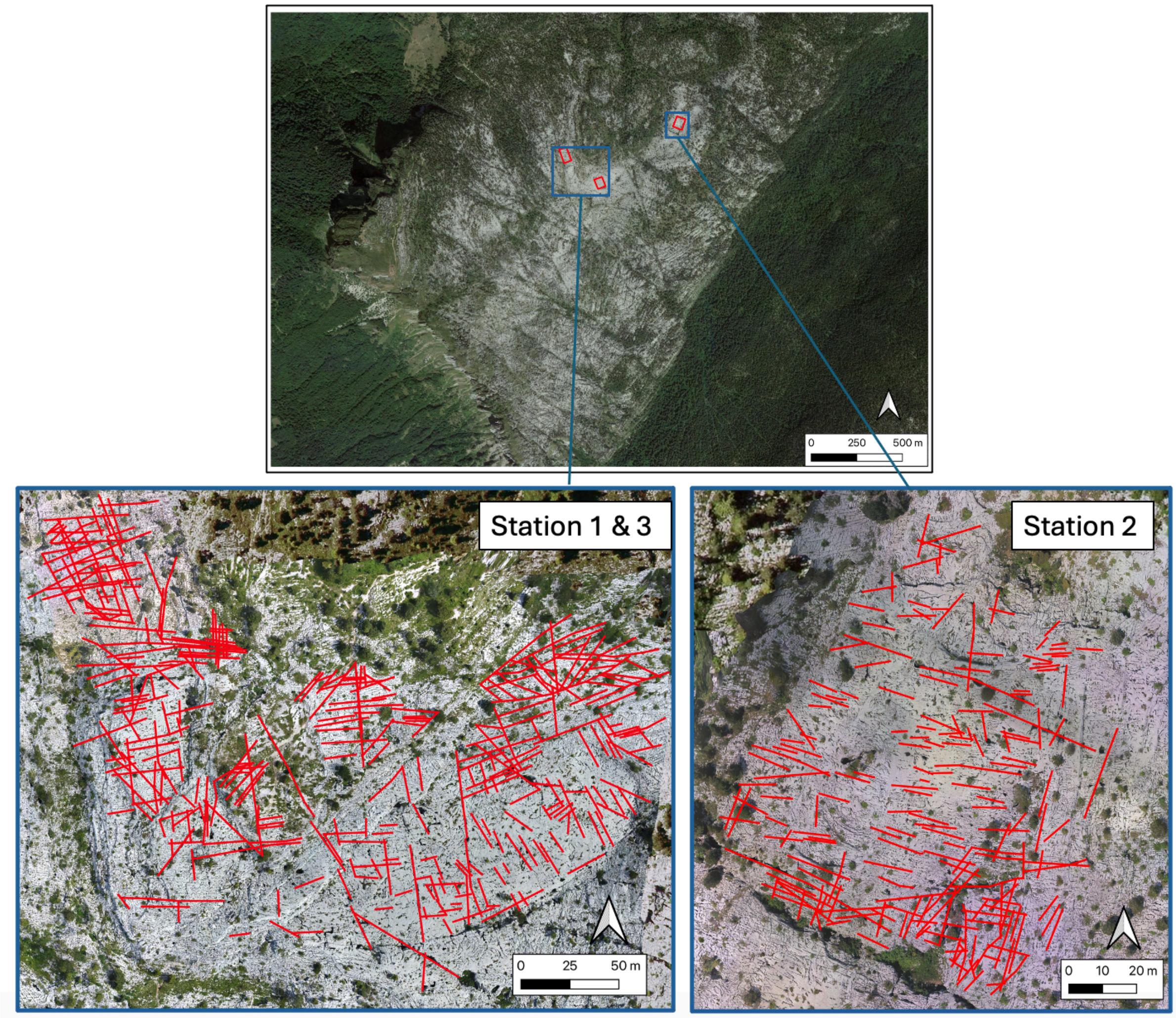

Figure A.2: Traced lineaments at 1:250 scale.

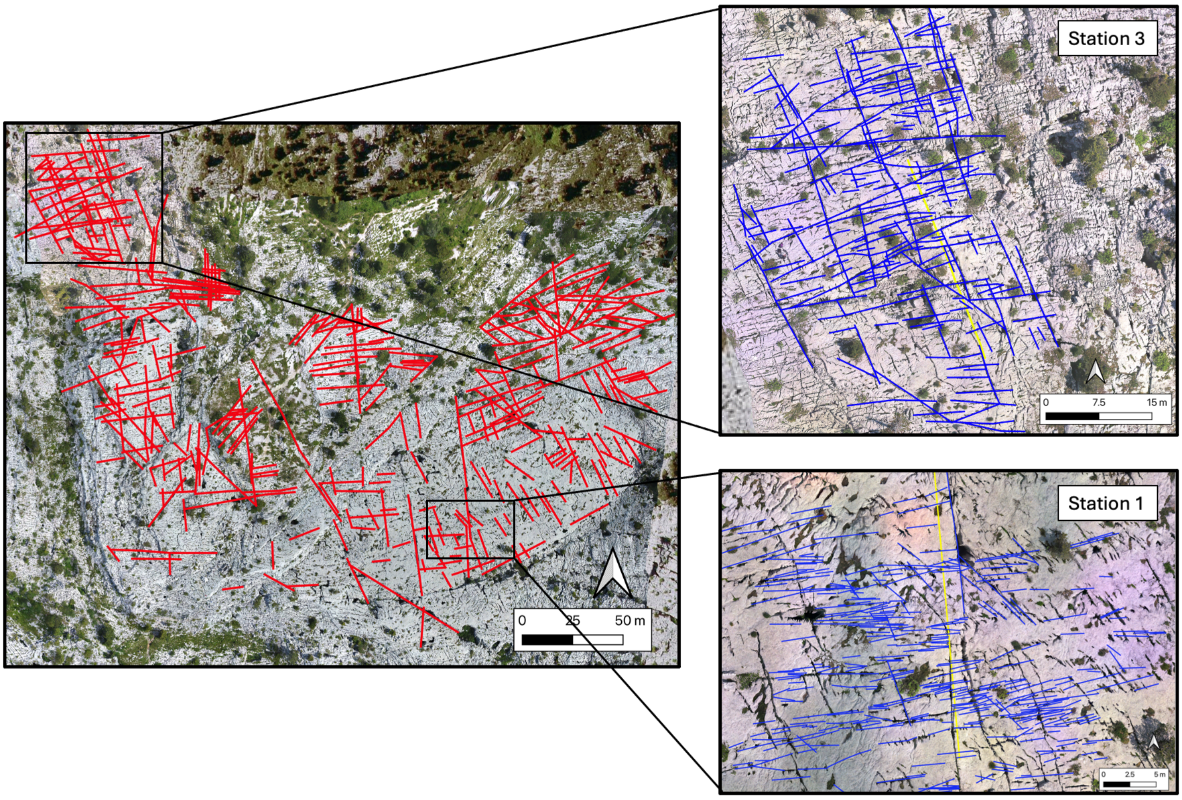

Figure A.3: Traced lineaments at Station 1 and 3 (at 1:10).